

Batool Akbar

Mathematical Modelling and Simulation of Flow in Collapsible Tubes

Master's thesis in Mechanical Engineering

Supervisor: Bernhard Müller

Co-supervisor: Sverre Gullikstad Johnsen and Paul Roger Leinan

June 2022

Batool Akbar

Mathematical Modelling and Simulation of Flow in Collapsible Tubes

Master's thesis in Mechanical Engineering

Supervisor: Bernhard Müller

Co-supervisor: Sverre Gullikstad Johnsen and Paul Roger Leinan

June 2022

Norwegian University of Science and Technology

Faculty of Engineering

Department of Energy and Process Engineering



NTNU

Norwegian University of
Science and Technology

EPT-M-2022

MASTER THESIS

for

Student Batool Akbar

Spring 2022

Mathematical Modelling and Simulation of Flow in Collapsible Tubes*Matematisk modellering og simulering av strømming i kollapserbare rør***Background and objective**

In many engineering applications, the two-way interaction between flowing fluids and flexible solid structures are of importance. In the biomechanics of the upper airways, the fluid-structure interaction (FSI) between flowing air and soft tissue is of specific interest due to the tendency of airway collapse during sleep (obstructive sleep apnea, OSA). E.g., it is believed that the Venturi effect occurring in narrow passages in the airway is responsible for the onset of OSA.

OSA affects approximately 20% of the adult population and is considered a major cause of reduced quality of life and mortality. A variety of treatment options exists, but today there are no available methods for predicting the outcome of the treatment. This master thesis will be part of a larger project, Virtual Surgery in the Upper Airways - New Solutions to Obstructive Sleep Apnea Treatment (VirtuOSA), which is a collaboration project between NTNU, SINTEF, and St. Olavs Hospital and is funded by the Research Council of Norway. The primary objective of VirtuOSA is to demonstrate the potential of a new patient-specific clinical tool based on mathematical models in predicting the response to OSA treatment.

The master thesis will contribute with establishing validated FSI models of flow in collapsible tubes, as a first step towards FSI modelling in realistic airway geometries. The objective of the master thesis is two-fold. First, a literature study on experimental and numerical studies of flow in collapsible tubes. Second, to establish, verify and validate a numerical two-way FSI model of flow in a collapsible tube, in available state-of-the-art CFD/FSI simulation software (e.g. ANSYS Mechanical, ANSYS Fluent and/or OpenFOAM).

The following tasks are to be considered:

1. A literature study on fluid-structure interaction of flow in collapsible tubes to find a suitable test case for verification and validation.
2. Establish a numerical model of the two-way fluid-structure interaction of flow in a collapsible tube.
3. Verification/validation of the numerical model against available numerical/experimental data.

-- " --

Within 14 days of receiving the written text on the master thesis, the candidate shall submit a research plan for her project to her supervisors.

When the thesis is evaluated, emphasis is put on processing of the results, and that they are presented in tabular and/or graphic form in a clear manner, and that they are analyzed carefully.

The thesis should be formulated as a research report with summary in English, conclusion, literature references, table of contents etc. During the preparation of the text, the candidate should make an effort to produce a well-structured and easily readable report. In order to ease the evaluation of the thesis, it is important that the cross-references are correct. In the making of the report, strong emphasis should be placed on both a thorough discussion of the results and an orderly presentation.

The candidate is requested to initiate and keep close contact with her academic supervisors throughout the working period. The candidate must follow the rules and regulations of NTNU as well as possible directions given by the Department of Energy and Process Engineering.

Risk assessment of the candidate's work shall be carried out, in cooperation with the supervisors, according to the department's procedures. The risk assessment must be documented and included as part of the final report. Events related to the candidate's work adversely affecting the health, safety or security, must be documented and included as part of the final report. If the documentation on risk assessment represents a large number of pages, the full version is to be submitted electronically to the supervisors and an excerpt is included in the report. Those who have a theoretical exercise only need to check this and fill out page 1 of the form provided by the Department of Energy and Process Engineering.

Pursuant to “Regulations concerning the supplementary provisions to the technology study program/Master of Science” at NTNU §20, the Department reserves the permission to utilize all the results and data for teaching and research purposes as well as in future publications.

The master's thesis is to be submitted in NTNU's examination system Inspera Assessment by 15:00 h on June 11, 2022.

- ☐ Work to be done in lab
☐ Field work

Department of Energy and Process Engineering, January 10, 2022

Bernhard Müller
Academic Supervisor

Sverre Gullikstad Johnsen
Co-supervisor

Paul Roger Leinan
Co-supervisor

Abstract

Obstructive sleep apnea (OSA) is a condition that intermittently blocks airflow through the upper airways in the human body during sleep for the people affected. This common condition can reduce sleep and life quality and even lead to serious health issues. The phenomenon is physically complex and has been investigated by researchers from multiple disciplines to understand it better and to find causes and treatments for OSA. The Venturi effect that occurs in the narrow passages in the upper airways can be responsible for the onset of OSA. Suppose the pressure difference between the inside and outside of the soft and flexible upper airway tissue is sufficiently high. In that case, it can lead to deformation and eventually obstruction of this part of the upper airways. The strong interaction between the fluid and solid in this case makes fluid-structure interaction (FSI) modelling highly relevant to understanding this phenomenon. Therefore, the objective of this thesis is to model the fluid-structure interaction in a collapsible tube.

Due to the complexity of numerical FSI modelling, a simple tube geometry has been chosen, rather than complex upper airway geometry, both for simplicity and in order to verify the model against previous works. Fluid flow with $Re = 128$ through a solid tube, with one part consisting of a linear elastic and flexible material, is modelled within Ansys Workbench 2021R2 [12]. The behaviour of the solid deformation is simulated with Ansys Mechanical 2021R2 [8] and the fluid flow is simulated with Ansys Fluent 2021R2 [5]. The two domains are connected through Ansys System Coupling 2021R2 [11] by transferring data between the shared surface of the solid and the fluid. The results are compared to results from Hazel and Heil [30], Huang [33], and Marzo et al. [45], displaying excellent agreement. With these results, the model created in Ansys Workbench 2021R2 [12] is verified, and the software's capability to solve this FSI problem is proved. Some additional simulations have also been done to investigate the effect of refining the meshes, changing convergence criteria, and increasing the Reynolds number.

Although others have solved collapsible tube problems, the value of a verified model in a commercial software is that it can easily be changed in terms of material properties, flow properties, and geometry than models explicitly created for a specific problem. Eventually, the goal will be to model realistic airways and predict the outcome of surgeries.

Sammendrag

Obstruktiv søvnapné (OSA) er en tilstand som midlertidig blokkerer luftstrømmen gjennom de øvre luftveiene under søvn for de som er rammet. Denne vanlige tilstanden kan redusere søvn og livskvalitet, og til og med føre til alvorlige helseproblemer. Fenomenet er fysisk komplekst og har blitt undersøkt av forskere fra ulike disipliner for å forstå OSA bedre og undersøke behandlingsmetoder. Venturi-effekten som oppstår i de trange passasjene i de øvre luftveiene kan være ansvarlig for utbruddet av OSA. Anta at trykkforskjellen mellom innsiden og utsiden av det myke og fleksible øvre luftveisvevet er tilstrekkelig høyt. Dette kan føre til at luftveiene deformerer seg og kollapser og dermed hindrer luft fra å strømme gjennom denne delen av de øvre luftveiene. Den sterke interaksjonen mellom fluidet og strukturen rundt gjør at fluid-struktur interaksjon (FSI)-modellering er svært relevant for å forstå dette fenomenet. Målet med denne oppgaven er derfor å modellere fluid-struktur interaksjonen i et kollapsbart rør.

På grunn av kompleksiteten til numerisk FSI-modellering er det valgt en enkel rørgeometri, fremfor kompleks øvre luftveisgeometri, både for enkelhets skyld og for å kunne verifisere modellen med tidligere arbeider. Fluidstrøm med $Re = 128$ gjennom et rør, hvor en del av røret består av lineært elastisk og fleksibelt materiale, er modellert i Ansys Workbench 2021R2 [12]. Oppførselen til røret er modellert med Ansys Mechanical 2021R2 [8] og fluidstrømningen med Ansys Fluent 2021R2 [5]. De to domenene kobles sammen gjennom Ansys System Coupling 2021R2 [11] ved å overføre data mellom domenenes delte overflate. Resultatene har blitt sammenlignet med resultater fra Hazel og Heil [30], Huang [33], og Marzo et al. [45], og viser utmerket samsvar. Med disse resultatene anses modellen laget i Ansys Workbench [12] å være verifisert og programvaren viser seg å ha sin evne til å løse dette FSI-problemet. Noen ekstra simuleringer er også gjort for å undersøke effekten av størrelse på mesh, konvergenskriterier og Reynolds-tall.

Selv om dette problemet er løst av andre tidligere, er verdien av å kunne løse det i en kommersiell programvare sammenlignet med modeller basert på egenskrevne koder for spesifikke problem, at parametre, geometri, og grensebetingelser enklere kan modifiseres. Etter hvert vil målet være å modellere realistiske luftveier og predikere utfallet av operasjoner på OSA-pasienter.

Preface

This thesis marks the end of five years of studying mechanical engineering at NTNU, specializing in fluid mechanics. Working on this thesis, where fluid mechanics, solid mechanics and numerics have been combined in the context of biomechanics, has been both very challenging and interesting.

I would like to express my great gratitude to my supervisor at NTNU, Bernhard Müller, and my co-supervisors from Sintef, Sverre Gullikstad Johnsen and Paul Roger Leinan for their supportive guidance and great enthusiasm for the project. Through frequent meetings, they have contributed with very useful feedback and valuable insights on challenges that showed up during the course of the thesis.

Table of Contents

List of Figures	ix
List of Tables	xi
List of Symbols and Abbreviations	xi
1 Introduction	1
2 Literature Review	3
2.1 Collapsible Tubes and the Starling Resistor	3
2.2 Previous Research on collapsible tubes	4
2.2.1 Experimental research	4
2.2.2 Analytical models	5
2.2.3 Numerical models	6
2.3 General theory of FSI	8
2.3.1 Monolithic vs. partitioned FSI approaches	8
2.3.2 One-way vs. two-way FSI modelling	9
2.3.3 Strongly-coupled vs. weakly-coupled methods	9
2.3.4 Comparison of coupling algorithms	10
2.3.5 Finite Element Method (FEM) and Finite Volume Method (FVM)	11
2.4 Challenges related to FSI in collapsible tubes	11
2.5 Commercial FSI tools	12
3 Mathematical and numerical model	15

3.1	Mathematical model	15
3.1.1	Governing equations for the structure	15
3.1.2	Governing equations for the fluid	16
3.1.3	Governing equations on fluid-solid interface	16
3.2	Numerical model	17
3.2.1	Approximation of structural equations	17
3.2.2	Approximation of fluid flow equations	18
3.2.3	Coupling algorithm	21
4	Simulation Setup	25
4.1	Problem statement	25
4.2	Main case simulation	26
4.2.1	Solid parameters	27
4.2.2	Fluid parameters	29
4.2.3	System Coupling Parameters	30
4.3	Simulations with increased Reynolds numbers	31
5	Results and discussion	33
5.1	Main case: Results and discussion	33
5.1.1	Comparison of results with previous numerical research	33
5.1.2	Qualitative comparison of results with experiments	33
5.1.3	Velocity and pressure distribution	36
5.2	Main case: Effects of changing simulation set-up	37
5.2.1	Mesh refinement study of the coupled system	37
5.2.2	Data transfer convergence	41
5.3	Effects of increasing the Reynolds number	42
6	Conclusions	49
7	Suggestions for future work	51
7.1	Future work on current model	51

7.2	Developing more complex models	52
Bibliography		55
A Details of main case model setup in ANSYS Workbench		I
A.1	System setup	I
A.2	Geometry	I
A.3	Transient Structural	II
A.3.1	Define solid material properties in Engineering data	II
A.3.2	Creation of the solid model	II
A.4	Fluid Flow (Fluent)	IV
A.4.1	Mesh	IV
A.4.2	Creation of the fluid model	V
A.5	System Coupling	VI
A.5.1	Couple participants	VI
A.5.2	Under-relaxation	VI
A.5.3	Analysis settings	VII
B Abstract accepted to ESB 2022		VIII

List of Figures

2.1	Example sketch of a Starling resistor in 2D.	4
2.2	Geometry in verification articles [30, 33, 45].	6
3.1	Illustration of the plane in which the 8 nodes of the quadrilateral shell element are located (left) and the degrees of freedom for one node (right).	17
3.2	Grid for a one-dimensional problem. See text for symbol descriptions.	19
3.3	Overview of FSI coupling scheme, where n is the current coupling iteration and c_1 and c_2 are the RMS convergence criteria for the data transfers. Flow chart created based on information given in Ansys System Coupling Users Guide [11].	23
4.1	Problem geometry schematic. See text for symbol descriptions.	26
4.2	Maximum deformation obtained for the solid tube with different element sizes of the mesh. Final external pressure exposure on the tube, in this case, is 0.3 Pa.	28
4.3	Fluid mesh from two views: Fluid flow inlet (left) and part of fluid wall (right). Images used courtesy of ANSYS, Inc.	29
5.1	Pressure along the centerline of the tube. Pressure and length down the tube are non-dimensionalized by dividing it by the flexural rigidity, $K = \frac{Eh^3}{12R^3(1-\nu^2)}$ and the undeformed radius, R , respectively. Note that $z/R = 0$ indicates where the flexible tube part begins and $z/R = 10$ is the flexible tube part's end. The horizontal line indicates the externally applied pressure, p_{ext}	34
5.2	The shape of one side of the tube wall (flexible part only) in the y-z-plane. Due to the symmetry, in this case, the shape is similar on the other tube wall side, and the shape of one side only is plotted. Both length scales are non-dimensionalized by the radius, R	34
5.3	Deformation of the flexible part of the tube from two views. Images used courtesy of ANSYS, Inc.	35

5.4	Pressure contour plots of flow in the y-z-plane (top) and the x-z-plane (bottom). Images used courtesy of ANSYS, Inc.	35
5.5	Velocity contour plots of flow in the y-z-plane (top) and the x-z-plane (bottom). Images used courtesy of ANSYS, Inc.	36
5.6	Pressure at tube centerline for simulations with three different mesh sizes. See Table 5.1 for mesh details.	38
5.7	Orthogonal mesh quality distribution of the initial and final deformed fluid mesh, respectively.	40
5.8	Cell equivolume skewness distribution of the initial and final deformed fluid mesh, respectively.	40
5.9	Pressure along the tube centerline for the different Reynolds number cases. Note that the pressure has been divided by the maximum pressure (i.e., inlet pressure) of each respective case to compare the curve's shape.	43
5.10	Pressure difference between the externally applied pressure and the pressure at flow centerline for the different Reynolds number cases.	44
5.11	Velocity vectors in a part of the y-z-plane (where the flexible part meets the downstream rigid part). The length of the vectors are normalized. The colours indicate the velocity magnitude with similar qualitative color-scaling as in Fig. 5.5. Images used courtesy of ANSYS, Inc.	44
5.12	Cross sectional views of the final tube configuration for the different Reynolds number cases. Images used courtesy of ANSYS, Inc.	45
5.13	Development of the buckling pattern through some time steps of the Re_5 -case. <i>time</i> is representing the external loads applied to the tube. Insert the <i>time</i> into Eq. 4.2 and 4.3 to find the externally applied loads. Images used courtesy of ANSYS, Inc.	45
5.14	Comparison of tube deformations for the different Reynolds number cases, viewed from the y-z-plane. Images used courtesy of ANSYS, Inc.	46
A.1	Systems and setup used in Ansys Workbench [12]. Image used courtesy of ANSYS, Inc.	I
A.2	Geometry in Ansys SpaceClaim [10], viewed from the y-z-plane. Image used courtesy of ANSYS, Inc.	II
A.3	Defining the tube material in Engineering Data in Ansys Workbench [12]. Image used courtesy of ANSYS, Inc.	II
A.4	Analysis Settings in Ansys Mechanical [8]. Image used courtesy of ANSYS, Inc.	IV

List of Tables

4.1	Parameters used in the main simulation, with units and dimensional values.	27
4.2	Overview of Grid Convergence Index (GCI) study for the fluid mesh.	30
5.1	Details of mesh sizes used and total computational time spent for the simulations in the mesh refinement study of the coupled problem. . .	38

List of Symbols and Abbreviations

Abbreviations

ALE	Arbitrary Lagrangian Eulerian
CFD	Computational fluid dynamics
CPAP	Continuous positive airway pressure
DOF	Degree of freedom
FEM	Finite element method
FSI	Fluid-structure interaction
FVM	Finite volume method
GCI	Grid convergence index
IAC	Interface artificial compressibility
IB	Immersed boundary
NED	Negative effort dependence
OSA	Obstructive sleep apnea
RMS	Root mean square

Symbols

Γ	Diffusion coefficient
μ	Dynamic viscosity
ω	Under-relaxation factor
ρ	Fluid density
ρ_m	Solid density
σ	Solid stress
σ^f	Fluid stress
θ	Rotation

ε	Strain
a, b	Perturbation load constants
A	Area
C	Stiffness tensor
D	Inner tube diameter
d	Displacement
D_h	Hydraulic diameter
E	Young's modulus
f^f	Fluid body forces
f^s	Applied forces on solid
h	Wall thickness
K	Flexural rigidity
K_b	Bending stiffness
L	Length
M	Mass ratio
P	Perimeter
p	Pressure
P_e	Non-dimensional downstream transmural pressure
Q	Volumetric flow rate
R	Inner tube radius
Re	Reynolds number
S	Source term
u	Fluid velocity
V	Volume
ν	Poisson ratio
W_0	Average inlet velocity

Chapter 1

Introduction

As numerical solvers have become more advanced and computational power has increased over the past few decades, the interest in developing more complex models with the ability to solve multiphysics problems has increased. Fluid-structure interaction (FSI) is an example of this, where the goal is to model systems with both fluids and structures, in which the motion and state of the domains are dependent on each other. Examples where this dependency is of importance can easily be found in the human body, such as the heart pumping, arteries deforming due to blood flow, and vibrations in the upper airways during snoring. In this thesis, fluid-structure interaction between a flexible tube and fluid flow through it is modelled. The purpose is to create a simplified model of what happens in the human upper airways during obstructive sleep apnea (OSA). Note that this thesis is a continuation of the author's project work [2] and hence relevant content has been re-used in this chapter, Chapter 1, and in Chapter 2.

OSA is a common condition amongst the adult population with varying degrees of seriousness, making the affected person frequently stop breathing during sleep, reducing their sleep and life quality. It can even lead to more serious health issues. One way of preventing OSA is the use of continuous positive airway pressure (CPAP) during the night [13]. It is also possible to reduce or diminish OSA with surgical intervention. However, in most cases, medical doctors and surgeons will not know if surgery will lead to improvement, no change, or worsening of the patients' sleep apnea. Researchers have therefore tried to numerically simulate processes in the upper airways to better understand what happens in the airways during sleep apnea. This paper is written as a part of the VirtuOSA project, a research collaboration between Sintef, NTNU, and St. Olavs hospital. The VirtuOSA project works toward solving the challenges stated, with the final goal of being able to predict the outcome of surgery on specific patients [62].

The Venturi effect occurring in the narrow passages in the upper airways can lead to OSA [58]. Some parts of the upper airways consist of soft, collapsible tissue. When air flows through these parts, a sufficiently high pressure difference between the inside and outside of the airway can lead to deformation of the soft tissue, making the airway even narrower. Due to the conservation of mass, the velocity increases in the narrowed parts of the channel. This again leads to a higher pressure difference

between the internal and external parts of the tissue, which deforms it even more. If the pressure difference is large enough, this sequence continues until the airway collapses and the person stops breathing. Eventually, when the brain realizes no air is flowing to the lungs, muscles are activated and the person starts breathing again [69], causing disturbed sleep.

This phenomenon is affected by, amongst other factors, the complex and patient-specific geometry and soft tissue material properties of the upper airways, the flexible and thin-walled airway material, and the strong interaction between the flowing air and the airway tissue. Due to this complexity, there are still many unanswered questions about the behaviour and occurrence of OSA. This study aims to create a numerical model of a collapsible tube using commercial software. Even though researchers have created in-house codes for solving similar problems, the value of solving them with commercial software is that it will likely be easier to apply the model to patient-specific cases in the future.

The model is created with Ansys Workbench 2021R2 [12] with a partitioned FSI approach by using Ansys Mechanical 2021R2 [8] to simulate the deformation of the solid and Ansys Fluent 2021R2 [5] for the fluid flow. The upper airway is represented as a cylindrical tube of linearly elastic material, while the fluid flow is incompressible with Reynolds number $Re_0 = 128$. The fluid-structure interaction is done via data transfers between the domains through Ansys System Coupling 2021R2 [11]. Some of the biggest challenges of using this FSI approach for such large deformation and strongly coupled FSI problems are data transfer instabilities and difficulties remeshing the fluid domain.

The results of the model created are compared to previous results from Hazel and Heil [30], Marzo et al. [45], and Huang [33] for verification purposes. Similar non-dimensional flow and structural parameters were used in the three mentioned studies.

Further simulations have also been done to investigate the effect of higher Reynolds number ($Re = 2 \cdot Re_0, 5 \cdot Re_0$) flows through the tube. In addition, simulations with different convergence criteria for the data transfer have been performed.

This thesis contains six chapters. Chapter 2 contains a detailed overview of previous research on collapsible tubes and theory on fluid-structure interaction, including the main challenges of FSI modelling and what separates different solvers and software. The governing equations in the mathematical model and the numerical model are presented in Chapter 3. Chapter 4 contains details of the model and settings used in Ansys [12]. Results and the discussion of them can be found in Chapter 5. Conclusions are given in Chapter 6. Finally, suggestions for future work are presented in Chapter 7.

Chapter 2

Literature Review

This chapter is taken from the author's project work [2](Chs. 2 and 3) with modifications and additions. The modifications include rewriting of some parts and changes in the structure of the text. In Subsection 2.2, some new research papers have been added. In Subsection 2.3, more coupling algorithms have been included. Subsection 2.5 about commercial software now includes more details about some software.

Collapsible tubes have been widely researched due to the many phenomena they occur in, such as in the human body. The nature of such channels is complex because of the large deformations, flexible material, complex geometries, and the strong interaction between the solid material and the fluid flowing through it. This literature review contains an overview of research done in this field.

2.1 Collapsible Tubes and the Starling Resistor

Attempts to understand what happens in collapsible tubes in the human body have led to the creation of many models with different simplifications and assumptions. For experimental purposes, Ernest Starling created the Starling resistor: a tube divided lengthwise into three parts, which is placed in a chamber with constant pressure [28]. A simplified sketch in 2D can be seen in Fig. 2.1. The first and third parts of the Starling resistor consist of rigid walls, while the middle part is of flexible material, making it prone to collapse. The volumetric flow rate is represented as Q in Fig. 2.1. p_{ext} , p_1 and p_2 in the figure are external, inlet and outlet pressures of the collapsible part, respectively. The pressure difference between the externally applied pressure and the fluid pressure will be referred to as the transmural pressure in the rest of the paper.

Let us now consider a three-dimensional Starling resistor, which initially (before any deformations) is a cylindrical tube. The pressure of the fluid decreases in the flow direction because of friction losses. The external pressure, however, is constant. Hence, the transmural pressure will vary along the length of the tube. A sufficiently high transmural pressure can lead to buckling of the flexible part. The resulting deformation then affects the flow velocity. The flow velocity increases with de-

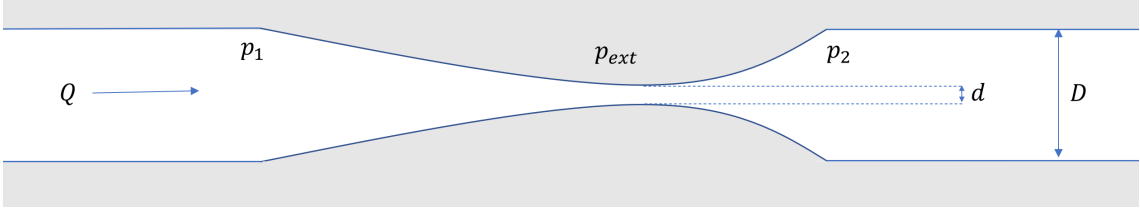


Figure 2.1: Example sketch of a Starling resistor in 2D.

creasing cross-sectional area, according to mass continuity. Furthermore, according to Bernoulli's equation, the Venturi effect implies that higher velocity gives lower pressure. Hence, the transmural pressure increases further, leading to larger deformations. When the transmural pressure is sufficiently high, opposite tube walls will touch ($d = 0$ in Fig. 2.1). This event will hereafter be referred to as a complete collapse. In other words, it is the first contact between opposite tube walls. Furthermore, a tube that can collapse will be referred to as a collapsible tube.

The cross-sectional shape of a deformed tube varies depending on how it buckles. The shape a cylindrical tube obtains after buckling can be categorized by how many folds appear in the cross section, also known as lobe modes. Which mode a tube achieves depends on many factors. Zhu et al. [73] showed that tube properties, such as its thickness, length, and diameter, as well as externally applied pressure, determined which mode the tube buckles to [71].

The Starling resistor and other collapsible tubes are used for experimental, analytical, and numerical modelling purposes. Their physics have been analyzed in 1D, 2D, and 3D, as steady and transient, with and without flow. Although the upper airways have complex geometry, it has many of the same qualities as the Starling resistor. The collapse of the upper airways during sleep apnea is believed to behave similarly to the Starling resistor's collapse. The middle part is similar to the part of the airways called the pharynx, as both are flexible and collapsible. The rigid walls represent the upstream nasal and downstream tracheal airways, which do not collapse [59]. The Starling resistor and similar models are therefore often used in the literature when considering the upper airways.

2.2 Previous Research on collapsible tubes

2.2.1 Experimental research

Numerous experiments have been done with collapsible tubes. Some important research will be reviewed here. As mentioned in Grotberg et al. [28], Bertram and coworkers have done important work in the experimental research of collapsible tubes, especially regarding oscillations that occur and their effect in physiological processes [17]. Spontaneous and self-excited oscillations were observed in the experiments, where silicone rubber was used for the solid tube and water as the working fluid. These oscillations indicated that pressure drop is not the only factor leading to collapse. Properties of the rigid parts, upstream and downstream of the col-

lapsible section, and the flow through them are also shown to be of importance when considering collapse [28, 42].

Other observed phenomena are flow limitation and pressure drop limitation [28]. If $p_1 - p_{ext}$ is kept constant, while $p_1 - p_2$ increases, a maximum value for Q will eventually be obtained. This is called flow limitation. If instead $p_2 - p_{ext}$ is kept constant, while Q is increased, this will lead to pressure drop limitation, meaning that $p_1 - p_2$ can not increase further.

Another phenomenon that can occur is negative effort dependence (NED). NED means that the flow rate decreases with increasing driving pressure, and it can occur after flow limitation has been reached at certain conditions [15, 39]. NED has been observed in the upper airways of some OSA patients as well [50].

As with all numerical methods, problems solved numerically with FSI also need to be compared to relevant experimental or analytical data to evaluate the accuracy of the results. Therefore, many researchers have conducted experiments with collapsible tubes to validate their numerical results. Examples can be found in Scroggs (2002) [60], Chouly et al. (2008) [22] and Le et al. (2019) [40]. Air was used as the working fluid in the two latter works, while Scroggs [60] used water.

Experiments, such as the work of Scroggs, visualize how collapsible tubes with flow through deforms (Figure 7.6 in [60]). It can be seen that the most deformed part is closer to the downstream end of the tube (as indicated in Fig. 2.1) rather than in the middle. This can be explained by friction losses through the tube, which leads to varying transmural pressure along the length of the tube.

2.2.2 Analytical models

Analytical models of collapsible tubes will not give a complete picture of the reality of the problem because of the many simplifications that are necessary to make in order to create a model. Some such models have been created and given interesting insights, even with many simplifying assumptions. Shapiro (1977) [61] made a 1D analytical model of steady flow in a collapsible tube. Amongst other simplifications, Shapiro used a simple so-called tube law to connect the tube's cross-sectional area to the transmural pressure. One of the conclusions of the study was that the flow could not be steady if the velocity is close to the speed of propagation because choking occurs [43]. Luo and Pedley (1995) [43] also created a 1D analytical model. It was compared to their numerical 2D model and they concluded that there was a good agreement between the two models for Reynolds numbers larger than or equal to 100.

As mentioned in section 2.1, a tube will collapse if the transmural pressure is sufficiently high. If considering a tube without flow through it and external pressure is applied, the transmural pressure becomes the externally applied pressure. For such a tube of linear elastic material with Young's modulus, E , Poisson ratio, ν , and wall thickness, h , the external pressure can, as done by for instance Marzo et al. [45]

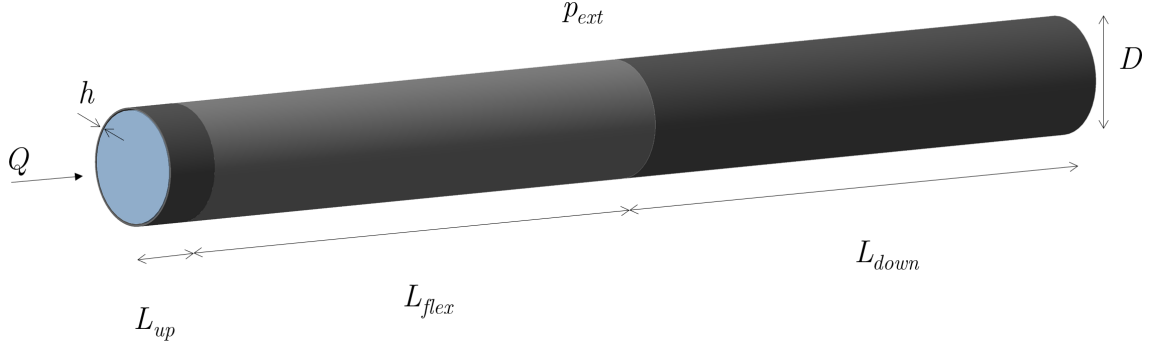


Figure 2.2: Geometry in verification articles [30, 33, 45].

and Flaherty et al. [26], be non-dimensionalized by

$$\overline{p_{ext}} = p_{ext}/K \quad (2.1)$$

where

$$K = \frac{Eh^3}{12(1 - \nu^2)R^3} \quad (2.2)$$

is the flexural rigidity of the thin-walled tube. It is introduced here as it will be used for non-dimensionalizing pressure in this study as well.

2.2.3 Numerical models

Models used for verification

There have been created many different numerical models in order to simulate collapsible tube events. The results obtained by Hazel and Heil (2003) [30], from their 3D finite-element method of steady viscous flow through a thin-walled tube, have been used for verification purposes for new models by other researchers, such as Marzo et al. (2005) [45], Zhang et al. (2018) [72] and Huang (2020) [33]. The model in the present study has also been verified by results from the works just mentioned. Therefore, this subsection is dedicated to describing their setups and parameters.

The non-dimensionalized parameters will be presented in Chapter 4. Figure 2.2 shows the geometric setup, which is common for all the works mentioned above. The tube is similar to the previously described Starling resistor. It consists of three parts. The middle part is flexible (of linear elastic material) and connected to rigid parts up and downstream of it.

Hazel and Heil [30] solved the steady incompressible Navier-Stokes equations for the flow and geometrically non-linear Kirchhoff-Love shell theory for the tube walls and used a partitioned approach to couple the two domains. Geometric non-linearity refers to structures where changes in geometry change their response, for instance, due to large deformations [48]. To use the shell theory, one has to assume, amongst other things, that the tube wall is thin ($h/R \ll 1$, where R is the inner tube

radius). Coupling between fluid and solid is done by transferring the pressure and traction forces from the fluid to the solid wall, and the solid wall deformations are transferred to the fluid domain.

In these works, it is desired that the tube deforms to a 2-lobed shape, which is assured in different ways. Hazel and Heil [30] prescribed radial displacements to specific points on the shell, while Marzo et al. [45] and Huang [33] applied a gradually decreasing perturbation load.

While Hazel and Heil [30] wrote their own code, Marzo et al. [45] used the finite-element program FIDAP, where the FSI problem-solving method is the partitioned approach. Huang used a finite element-immersed boundary-lattice Boltzmann method (FE-IB-LBM). Zhang et al. [72] created a novel arbitrary Lagrangian-Eulerian (ALE) method with a frontal solver. In the frontal solver, the equations are solved on a smaller portion of the elements in order to avoid the creation of large sparse matrices [72].

Zhang et al. [72] used the setup described for verification of their solver. However, the main focus of their work was to examine the collapsible tube problem using a tube with different hyperelastic materials and to study 3-mode buckling.

Other models

Before the numerical 3D models mentioned above were created, the problem was solved in 2D. Rast (1994) [57] simulated a 2D steady rigid tube, with one section replaced by a thin membrane. Rast successfully developed a monolithic non-linear solver, which solved the incompressible Navier-Stokes equations and membrane equations for the thin membrane. Rast emphasized that there is uncertainty in using steady solvers for such problems. Luo and Pedley (1996) [44] used the numerical approach of Rast to create a steady 2D solver. Further, an unsteady solver was created to investigate the steady solution's instabilities. The results revealed that instabilities occurred in the steady solution when the membrane tension was critically low.

Like the ones just mentioned, many of the earlier works in the field have created their own solvers for the specific problem. This approach has also been used more recently and can be seen in Ha et al. (2017) [29], where an in-house monolithic approach to a collapsible tube problem was created. However, it has become more common to simulate fluid-structure interaction with commercial software. Ha et al. [29] compared their in-house solver with the partitioned approach of Ansys [12].

Scroggs (2002) [60] used LS-DYNA, an explicit software, which can account for fluid-structure interaction. He did experiments and 3D numerical analysis on a collapsible tube with water flowing through it. He successfully did both steady and unsteady high Reynolds number numerical analysis in LS-DYNA, which corresponded well with the experimental results. In addition, detailed stress distributions along the tube walls and fluid flow patterns were displayed.

Simulating the airways with realistic geometries has become more feasible with com-

mercial tools. Le et al. (2019) [40] used Ansys Workbench [12] to simulate deformations of the upper airways with realistic geometry. The results were compared to their own experiments, and conclusions included that the pressure-flow curve was independent of the different breathing patterns tested. Another example of fluid-structure interaction in realistic airways can be found in Pirnar et al. (2015) [53].

Subramaniam et al. (2017) [64] computed the deformation of the upper airway tissue induced by airflow in an OSA patient. They concluded that using the $k - \omega$ SST turbulence model and a Neo-Hookean hyperelastic material model worked well in predicting the deformations.

Chang et al. (2018) [20] simulated the airflow in the airways using both computational fluid dynamics (CFD) alone and FSI before and after surgery of OSA patients. The surgeries improved their sleep apnea conditions, which could be seen in comparing the numerical simulations before and after surgery. Both CFD and FSI simulations indicated that less effort was needed to breathe after surgery. However, the FSI simulations showed that deformations in the airways were reduced after surgery, a result that could not be obtained from CFD alone.

The works mentioned above solve their respective problems using different solvers and simplifications, showing that there are many different ways to investigate the behaviour of collapsible tubes. It also reveals that many challenges still need to be solved to fully understand collapsible tube behaviour and the upper airways during sleep apnea. In most of the works, the tubes are not completely collapsed, i.e., opposite tube walls touching. This can be because the software or code cannot account for the large domain reduction and following hole or split in the fluid mesh.

2.3 General theory of FSI

The Starling resistor and collapse in the upper airways are prime examples of FSI problems because the behaviour of the solid and fluid are highly affected by each other. FSI problems are characterized by the behavioural dependency between fluid and solid, which are connected at one or more surface interfaces. Governing equations of the fluid and solid domain must be satisfied simultaneously at this interface. There are many approaches to solving FSI problems numerically and which one is chosen depends on the specific problem to be solved. This section presents some common ways to differentiate between types of solvers and methods.

2.3.1 Monolithic vs. partitioned FSI approaches

The numerical approximation of FSI can be divided into two categories on a high level: *partitioned* (or staggered) methods and *monolithic* methods [14]. The latter solves the fluid and solid equations in a single mathematical framework. Monolithic approaches are also called fully-coupled because the governing equations of the solid and fluid are solved simultaneously. In partitioned solvers, the governing equations are solved separately for the fluid and the solid, and they are connected

through a coupling mechanism. One of the advantages of partitioned approaches is that existing and well-tested solvers can be used for each domain, for example, the finite volume method (FVM) for the fluid and finite element method (FEM) for the solid [29]. Ha et al. [29] compared partitioned and monolithic methods for fluid-structure interaction in blood vessels. They concluded that their in-house monolithic approach had a better convergence behaviour and lower CPU (central processing unit) requirements than the partitioned approach used.

As partitioned solvers have separate meshes for the fluid and solid, a common approach is to use body-fitting and non-overlapping meshes. This method requires frequent remeshing of the fluid domain when the solid deforms. This factor and the data transfer needed between solid and fluid can lead to high computation time.

Ha et al. [29] also stated that problems with strong FSI, which are prevalent for collapsible tubes, should be modelled with monolithic solvers due to convergence issues with partitioned solvers in such cases. However, as mentioned in the literature review, partitioned solvers have previously given satisfying results [20, 40].

2.3.2 One-way vs. two-way FSI modelling

One of the first things to consider before setting up a partitioned FSI model is whether it needs to be simulated with a *two-way* coupling or if a *one-way* coupling is sufficient. A one-way coupling includes data transfer only from one domain to the other. Typically this method can be used when deformations of the solid are considered small enough for the fluid domain to stay unaffected [25]. In such cases, the governing equations of the fluid are solved, and pressure forces are transferred to the solid. However, the deformations of the solid are not transferred back to the fluid. In a two-way FSI, the solid and fluid significantly affect each other, implying that data transfer is necessary in both directions, i.e., from fluid to solid and solid to fluid. Compared to one-way coupling, this method requires more data transfer, resulting in higher computation times. However, a two-way coupling is a more accurate representation of reality. To simulate collapse in the upper airways, if a partitioned approach is used, a two-way FSI is necessary because the behaviour of the flow and the surrounding tissue are highly affected by each other.

2.3.3 Strongly-coupled vs. weakly-coupled methods

When considering unsteady problems, two-way partitioned methods can again be divided into two categories: strongly or weakly coupled methods. With a weak coupling, also called iterative coupling, the fluid and solid solvers use different time steps and require one solution for each problem at each coupling time step. A strong coupling, however, executes multiple iterations within one coupling time step for both solvers, which is more computationally expensive, but in turn, ensures energy conservation at the interface and can increase stability [66].

2.3.4 Comparison of coupling algorithms

For FSI simulations in Ansys Workbench 2021 R1 [12] (with Ansys Mechanical [8], Ansys Fluent [5] and Ansys System Coupling [11]), which is the tool used for the simulations in this study, the fluid and solid equations are solved separately and coupled through data transfer, i.e., it is a partitioned solver. Lagrangian and Eulerian descriptions are used for the solid and fluid, respectively. The Lagrangian description is common in structural mechanics and means that the mesh deforms with the material movements [14]. The Eulerian description is common when considering fluids, as the mesh stays still while the fluid flows through it. When the solid deforms, this combination of descriptions requires that the fluid domain is frequently remeshed. Since the motion of the fluid domain is not known, FSI problems can be viewed as a three-field problem, where the unknown fields are the solid, the fluid, and the fluid domain motion [14].

Before going into details of the partitioned coupling algorithm used in the present study, some common coupling methods will be reviewed.

The Arbitrary Lagrangian Eulerian (ALE) formulation consists of a Lagrangian description of the solid domain and an Eulerian description of the fluid domain. The ALE method, developed by Hirt et al. (1974) [31], can add flexibility and robustness to the simulation because the fluid domain has the options of both moving with the fluid or being in a fixed position. Although this method provides flexibility, it still requires frequent remeshing of the domains in the case of large deformation.

The immersed boundary (IB) method, first developed by Peskin (1972) [52], is an alternative to body-fitting approaches, for example, ALE. This method uses an Eulerian description for the fluid, a Lagrangian description for the solid, and a nonconforming discretization along with the fluid-structure interface. The main challenge with this method is the coupling of the Eulerian and Lagrangian variables at the interface, such as calculating the stresses [24]. However, it avoids the need for frequent remeshing [27].

The Cartesian cut-cell method is another alternative to body-fitted approaches. The method includes using a Cartesian background grid for the flow domain while cutting solid bodies out of the background mesh [34]. This leads to a sharp interface for the flow domain, which assures conservation of mass, momentum, and energy [51].

The Interface Artificial Compressibility method (IAC) consists of assigning artificial compressibility to an incompressible fluid in order to mimic the elastic behaviour of the solid [56]. It is possible to add the artificial compressibility to the entire fluid domain, called AC, or only close to the fluid-solid interface, then called IAC. IAC can improve convergence issues in some FSI problems.

2.3.5 Finite Element Method (FEM) and Finite Volume Method (FVM)

FEM and FVM have been mentioned in the previous sections and will be briefly presented here. Both are computational methods where the domain considered is divided into a finite number of smaller parts, often referred to as elements in FEM and control volumes in FVM.

Both methods start by formulating integral equations weighted with so-called test functions and integrating them over the domain. In FVM, one constant test function is chosen for each cell. On the other hand, in FEM, polynomials are instead chosen for each element. There are many different ways of solving the equations further for both FEM and FVM, and in some cases, the methods are, in fact, very similar. FVM has commonly been used for computational fluid dynamics (CFD), but FEM can also be implemented for fluid problems [23].

2.4 Challenges related to FSI in collapsible tubes

As mentioned by Bazilevs et al. [14], challenges related to any numerical discretization of a single-field problem, such as accuracy, stability, and computational time naturally also occur when solving multi-field problems, like FSI, numerically. They are often more challenging in FSI problems due to the interface between fluid and solid and the domain interactions.

Handling the fluid-solid interface is necessary for all FSI problems. In the case of collapsible tubes, the large solid deformations that occur are a significant computational challenge. If a partitioned approach is used, the large deformations can require frequent remeshing of the fluid domain. The challenge with a moving fluid mesh in FSI is that the new fluid boundary and deformation of the fluid mesh are not known. In addition, an interpolation of the solution from the old to the new mesh must be done [14]. The forces must also be interpolated when transferred from the fluid to the solid in a partitioned solver due to non-overlapping meshes.

Data transfer instabilities can arise in partitioned solvers, especially when large deformations are involved [21]. This happens because the fluid boundary is unknown, and the data must be interpolated both ways. The direction of the solid deformations can change due to this, creating the instabilities (see Fig. 9 in Chimakurthi et al. [21] for a describing illustration of how data transfer instabilities can happen). It is possible to diminish such instabilities by applying different stabilization techniques, such as under-relaxation of the data transfers or ramping the loads to apply them gradually. The downside of such techniques is that more computational effort is required.

In addition, the literature review revealed that the behaviour of collapsible tubes could include oscillations, which can be challenging to catch in numerical modelling [17] because of restrictions on time resolution. This can also create challenges related to validating numerical models, as experiments are also challenging to conduct on

collapsible tubes. The complex flow behaviour can make measuring and monitoring the flow pattern difficult.

Additional challenges appear if we consider numerically simulating the event of OSA in the upper airways. In that case, it can be challenging to state the problem and parameters, such as creating a material model that mimics the upper airway tissue, creating the complex geometric domain, and discretizing them. In addition to the geometric non-linearities of the problem, the materials are often hyperelastic, introducing material non-linearities as well. The breathing pattern and boundary conditions of the flow and the external load on the airway tissue might be hard to measure and determine.

2.5 Commercial FSI tools

The use of commercial tools to solve FSI problems has become quite common. Although Ansys Workbench [12] (with Ansys Mechanical [8], Ansys Fluent [5], and Ansys System Coupling [11]) have been used for simulations in this study, other commercial solvers were also investigated and considered for the simulations.

It is possible to solve FSI problems in Ansys Fluent [5] alone, also known as intrinsic FSI. The tool has some limitations; for instance, Young's modulus and Poisson's ratio for the solid must be constant. The approach is partitioned.

ADINA [1] is a tool that can solve FSI problems with both a monolithic and partitioned approach [1]. Structural equations are solved with FEM using a Lagrangian formulation. The Navier-Stokes equations for the fluid can be discretized with either FEM or FVM. For FSI, an ALE formulation can be applied [71]. Examples of use of ADINA [1] for FSI of collapsible tubes can be found in the literature [18], [65], [37].

LS-DYNA is a tool made to solve non-linear transient dynamic finite element analysis, which uses explicit time integration. Typical applications can be the simulation of car crashes or explosions [41]. It is also possible to do FSI with the ALE approach in LS-DYNA. Scroggs [60] used LS-DYNA to simulate a collapsible tube, and collapse was obtained. One of the objectives of his thesis was to validate LS-DYNA as an FSI tool. He concluded that it was qualitatively accurate but could not draw the same conclusion for its quantitative properties due to some errors related to uncertainty.

Other FSI tools include Abaqus [63] (coupled with a CFD-solver) and the open source software, OpenFOAM [49]. Both can apply the partitioned approach for FSI. The advantage of open source software is that models created can be used and modified by anyone regarding access to the software. On the downside, it has no user interface, making the required knowledge to use the software higher than for software with user interfaces.

From this brief review, it can not be concluded whether one of the mentioned tools is better than another. Many of them have similar qualities, as they are partitioned

and capable of two-way FSI. Ansys Workbench [12] was chosen because the tools are widely used and contain many functions, so models can easily be adjusted. In addition, its user interface makes it easy for the user to visualize how the solid and fluid are connected. As mentioned in Section 2.2, FSI on collapsible tubes have been obtained with these tools, even with realistic airway geometries. In addition, since it is a partitioned solver, it is possible to look into each domain, i.e., the fluid and solid domain, separately before coupling them. There are also three different stabilization techniques in Ansys System Coupling [11], which are of great use in systems like collapsible tubes because the high dependency between the two domains can create large instabilities. The three techniques are under-relaxation, ramping, and the use of a Quasi-Newton approach to the data transfer [11](p. 258). Even if all techniques are not used in this work, it adds flexibility for future work.

Chapter 3

Mathematical and numerical model

3.1 Mathematical model

3.1.1 Governing equations for the structure

The governing equations for the linear elastic tube are listed below, where Eqs. 3.1 are the momentum equations, Eqs. 3.2 are the strain-displacement equations and Eqs. 3.3 are the constitutive equations, which in this case are based on Hooke's law. In the equations, the indices i and j represent the directions, (x, y, z) , and repeated indices imply summation over all index values.

$$\frac{\partial \sigma_{ij}}{\partial x_j} + f_i^s = 0. \quad (3.1)$$

$$\varepsilon_{ij} = \frac{1}{2} \left(\frac{\partial d_i}{\partial x_j} + \frac{\partial d_j}{\partial x_i} \right). \quad (3.2)$$

$$\sigma_{ij} = C_{ijkl} \varepsilon_{kl}. \quad (3.3)$$

σ_{ij} is the Cauchy stress tensor, and f_i^s are the applied forces, which in this case are the externally applied pressure loads and the traction forces from the fluid interface. The strain tensor is denoted by ε_{kl} and the displacement by d_i . Finally, C_{ijkl} is the fourth order stiffness tensor [45].

Equation 3.3 can be rewritten for the isotropic linear elastic material as

$$\sigma_{ij} = \frac{E}{1+v} \left(\frac{v}{1-2v} \text{Tr}(\varepsilon_{ij}) I + \varepsilon_{ij} \right) \quad (3.4)$$

where E and ν is the material Youngs modulus and Poisson ratio, respectively. I is the identity matrix and $Tr(\varepsilon_{ij})$ represents the trace of the matrix, ε_{ij} .

3.1.2 Governing equations for the fluid

The flow is steady and governed by the Navier-Stokes equations. The fluid is assumed to be incompressible and Newtonian. Therefore, the continuity equation simplifies to

$$\frac{\partial u_i}{\partial x_i} = 0, \quad i = 1, 2, 3, \quad (3.5)$$

where u_i is the flow velocity. Constant fluid density and viscosity yields the momentum equations,

$$\rho u_j \frac{\partial u_i}{\partial x_j} = -\frac{\partial p}{\partial x_i} + \mu \frac{\partial^2 u_i}{\partial x_j \partial x_j} + f_i^f, \quad i = 1, 2, 3, \quad (3.6)$$

where f_i^f , ρ , p , and μ are the body forces per unit volume applied to the fluid, fluid density, pressure, and dynamic viscosity, respectively. The flow is assumed to be laminar with constant viscosity. For later reference, the term on the left-hand side is the convection term, while the second term on the right-hand side is the diffusion term.

No-slip at the stationary walls gives

$$u_{i,wall} = 0, \quad i = 1, 2, 3. \quad (3.7)$$

3.1.3 Governing equations on fluid-solid interface

Two necessary conditions need to be fulfilled at the fluid-solid interface. The first one is the so-called geometrical compatibility [68]:

$$d^f = d^s \quad \text{on} \quad \Gamma \quad (3.8)$$

where d^f , d^s , Γ are the fluid and solid displacements and the interface surface, respectively.

The second condition is traction equilibrium:

$$\sigma^f n = \sigma n \quad \text{on} \quad \Gamma \quad (3.9)$$

where σ^f and σ are the stresses of the fluid and solid, respectively. n is the normal unit vector to the interface Γ .

Note that a common additional condition for this type of FSI problem with no-slip at the fluid wall would imply that the velocity of the fluid must be equal to the rate of displacement of the solid on the interface [32], [68]. However, this being a steady simulation, the wall is stationary when the fluid flow is approximated, which is why Eq. 3.7 is sufficient.

3.2 Numerical model

Theory behind the numerical method used for the simulations done within Ansys Workbench [12] will be presented in this section.

3.2.1 Approximation of structural equations

The behaviour of the solid is approximated with Ansys Mechanical [8], in the Ansys Workbench [12] system named Transient Structural. This system is used to create a step-wise system coupling where each step indicates an increase in external pressure load in order for the deformations to happen slowly. However, time integration is turned off, as the solution wanted is steady and therefore time dependency is not necessary. Ansys Mechanical [8] solves equations with FEM. The solid domain is first discretized into quadrilateral and quadratic shell elements. A quadratic element implies that there are nodes on the mid sides of the element and on the corners. Hence, these elements each consist of 8 nodes. Furthermore, each node has six degrees of freedom (DOF), displacements in all three directions (d_x, d_y, d_z) and rotations in all three planes ($\theta_x, \theta_y, \theta_z$). See Fig. 3.1 for illustrations of the degrees of freedom at each node and of one shell element with the eight nodes marked. Although not illustrated, the shell element is assigned a thickness.

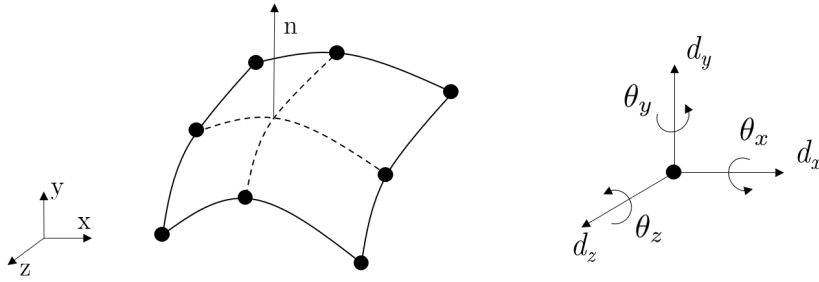


Figure 3.1: Illustration of the plane in which the 8 nodes of the quadrilateral shell element are located (left) and the degrees of freedom for one node (right).

Each DOF is represented by one unknown equation (Eq. 3.1). Therefore the total number of degrees of freedom for the entire solid domain becomes six times the number of nodes. The stiffness matrix for each element then consists of $N \times N$ terms, where N is the number of nodes multiplied by the number of DOFs at each node. Stiffness matrices for all the elements are combined reasonably, considering boundary conditions and element connections to create the overall stiffness matrix. An

element's stiffness matrix represents its resistance to deforming; the resistance one node encounters when it moves with respect to the other nodes.

In-depth details of how the full stiffness matrix is formed will not be included due to the long derivations and the intricate methods used by Ansys Mechanical [8]. However, it is worth mentioning that the stiffness matrix for shell elements can, in simple terms, be viewed as a superposition of in-plane stress analysis and an out-of-plane bending formulation. See references [54] and [55] for details on how both types of matrices are set up.

The stiffness matrix is updated at every equilibrium iteration, as a full Newton-Raphson method is used. Because pressure differences drive the collapse in this case, unsymmetrical pressure load stiffness matrices can improve convergence, and this is also turned on. In addition, line search is turned on, reducing instabilities by improving the Newton-Raphson solution by scaling the solution vector with a value between 0.05 and 1. In this case, the value is automated by Ansys Mechanical [6](Ch. 8.6.3.1.2).

When large deflection effects are turned on in Ansys Mechanical [8], the direction of the pressure load changes so that it stays normal to the surface. The tube deformations are large in this case and the tube shape changes throughout the simulation. Due to this, the stiffness changes, i.e., geometric non-linearity is present. Large deflection effects must therefore be considered.

The solver type in Ansys Mechanical [8] chosen is direct. Solver type defines how the equations will be solved for the implicit solver. The direct approach, also known as Sparse, uses Gauss-elimination to solve the equations [7](Ch. 14.7).

3.2.2 Approximation of fluid flow equations

Approximation of fluid flow is done in the software Ansys Fluent [5]. The partial differential equations presented in Subsection 3.1.2 are first discretized. Further, the domain is transformed into a mesh consisting of many cells. The discretized equations are then solved for each cell, dependent on its neighboring cells' properties. Where in the cell each property is stored or needed depends on the property considered. In Ansys Fluent [5], discrete values are stored at the cell center. Fluxes, however, must be obtained at the cell faces. These are obtained from interpolation from cell center values, which is done with upwind schemes [4](Ch. 24.3.1).

The discretizations and matrix equations that are solved in Ansys Fluent [5] for this problem will not be presented because there are many equations. With three dimensions, one discretization becomes quite lengthy. However, to understand the essence of the FVM method in Ansys Fluent [5], a simple discretization of a one-dimensional steady convection-diffusion equation is presented below ([35],[67](Ch. 5)).

For a simplified explanation of the upwind method and central differences, let us consider the following general steady convection-diffusion equation in integral form,

$$\int_{\partial\Omega} \rho \Phi \vec{u} \cdot \vec{n} dA = \int_{\partial\Omega} \Gamma \vec{\nabla} \Phi \cdot \vec{n} dA + \int_{\Omega} S_{\Phi} dV, \quad (3.10)$$

for any property Φ with diffusion coefficient Γ , density ρ and velocity \vec{u} . S_{Φ} is the source term of Φ per unit volume. Ω is the fluid domain, and $\partial\Omega$ represents the domain's boundaries.

If we then consider a one-dimensional problem of the given equation, Fig. 3.2 displays a part of the mesh with three neighboring cells. The discretization then becomes

$$(\rho u A)_e \Phi_e - (\rho u A)_w \Phi_w = \left(\Gamma A \frac{d\Phi}{dx} \right)_e - \left(\Gamma A \frac{d\Phi}{dx} \right)_w + \bar{S}_{\phi} V_P \quad (3.11)$$

Since values at cell centers are stored, the diffusive term values at the cell boundaries can be found directly from the cell center values with central differences:

$$F_e \Phi_e - F_w \Phi_w = D_e (\Phi_E - \Phi_P) - D_w (\Phi_P - \Phi_W) + S_U + S_P \Phi_P \quad (3.12)$$

where S_U and S_P are source terms.

$$F_{e/w} = (\rho u A)_{e/w}, D_{e/w} = \frac{A_{e/w} \Gamma_{e/w}}{\delta x_{PE/WP}} \quad (3.13)$$

with $\delta x_{PE} = x_E - x_P$, $\delta x_{WP} = x_P - x_E$

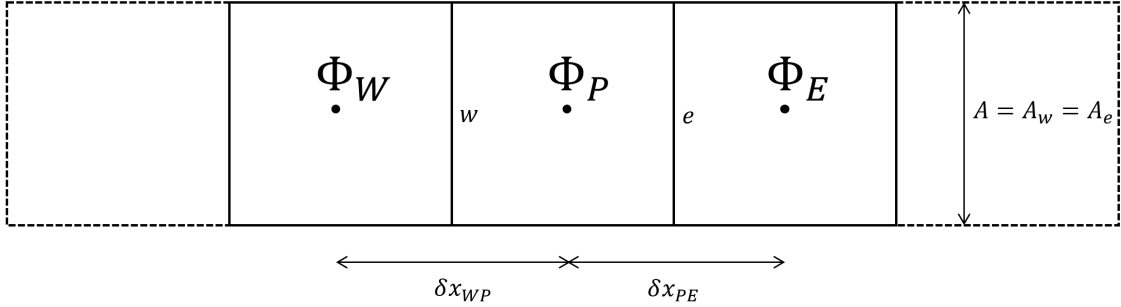


Figure 3.2: Grid for a one-dimensional problem. See text for symbol descriptions.

The convective term must, however, as mentioned, be interpolated from the cell center values. Using the first-order upwind method simply sets the value on a face equal to the cell center value in the upstream cell. For example, if $\Phi_e > 0$, $\Phi_e = \Phi_P$, while if it is less than 0, it will be $\Phi_e = \Phi_E$. In general, it can be written as

$$F_e \Phi_e = \frac{1}{2} [F_e \Phi_P + F_e \Phi_E - |F_e| (\Phi_E - \Phi_P)]. \quad (3.14)$$

Using the same principle of upwind cell center values, a similar expression can be found for $F_w \Phi_w$. The same principle is used in Ansys Fluent [5] for three-dimensional

problems, where convective terms are solved with upwind schemes, and diffusive terms are solved with central differencing. If a first order central differencing scheme would be used on the simple 1D case above, the property Φ at the east face could be found by:

$$\Phi_e = \frac{1}{2}(\Phi_E + \Phi_P). \quad (3.15)$$

For the simulations in this study, a second-order upwind method has been chosen for the discretization of the momentum equations (Eq. 3.6). The difference from the first order upwind method mentioned is that cell face values are obtained by summation of the cell-centered value, and its gradient in the upstream cell [4](Ch. 24.3.1.2). The gradient calculation is described later. Second-order upwind is chosen because an unstructured grid is used (tetrahedral elements), which means that the flow is not aligned with the mesh, and using only first order accurate upwind method increases the numerical diffusion error [4](Ch. 32.2.1).

For secondary diffusion terms and velocity derivatives, of which both can be found in Eq. 3.6, gradient evaluation is necessary [4](Ch. 24.3.3). In this case, the least squares cell-based method is used for gradient evaluation, a technique where the solution is assumed to vary linearly along with cell center values.

Pressure is stored in the cell centers. Therefore, interpolation is required to obtain pressure values at cell faces. In this case, this is done with the second order scheme, which uses a central differencing scheme [4](Ch. 24.4.1.1).

Using central difference alone for the pressure is insufficient, as the pressure field is unknown. Therefore, an iterative pressure-velocity coupling is done to improve an initial guess of the pressure field. In this case, the coupled algorithm is used, which means that the momentum and continuity equations are solved together [4](Ch. 24.4.3.3). This coupling is chosen as it is superior to segregated approaches in terms of efficiency and robustness for steady state cases.

All equations above are simplified versions of what Ansys Fluent [5] uses to solve the governing equations. Problems with three dimensions and unstructured meshes require more complex equations where directional vectors are important. Regardless, the above equations still give some understanding as to how the flow is approximated.

The methods mentioned above are implemented to approximate the solution of the governing equations for a given mesh. Since the mesh, in this case, is changing as deformations increase, the mesh is updated throughout the simulation.

The steady state simulation for the current problem will run through multiple iterations until convergence is reached or if the set maximum number of iterations is reached. Convergence is evaluated by monitoring the residuals for continuity and velocities per iteration and is reached when the residuals become below the set criteria.

3.2.3 Coupling algorithm

Figure 3.3 shows an overview of how Ansys System Coupling [11] interacts with Ansys Fluent [5] and Ansys Mechanical [8] in order to obtain fluid-structure interaction. Overall, the simulation consists of a finite number of coupling steps. In this case, the uniform external pressure on the tube increases while the perturbation load decreases, with each coupling step, with the final values of the uniform and perturbation loads becoming p_{ext} and 0, respectively. Within each coupling step, coupling iterations are executed until convergence (or maximum number of iterations) is reached. When an entire coupling iteration is converged, the coupling step is complete, and the simulation can move on to the next step.

Within each iteration, multiple processes take place, as can be seen in the figure. In short, Ansys Fluent [5] solves the fluid flow equations until convergence or until maximum iterations are reached. The forces on the fluid boundary are then transferred via system coupling to the solid domain. Because the two meshes are not entirely aligned, interpolating the forces between the surfaces is necessary. Then the solid equations are solved until convergence. The solid displacement is then transferred to Ansys Fluent [5], which remeshes the fluid domain accordingly.

For a coupling iteration to converge, the solution within both solvers must be converged. In addition, the two data transfers must also converge. The convergence of data transfers is evaluated by comparing the data transfer values of the current iteration to the previous iteration (within or across the coupling steps). In the current study, the method used to compare successive iterations is by calculation of a global root mean square (RMS) for the data transfer value, ϕ , defined as [11](p. 235):

$$RMS(\phi^n, \phi^{n-1}) = \sqrt{\frac{1}{k} \sum_{i=1}^k \bar{\Delta}^2} \quad (3.16)$$

where k is the number of data transfer values and $\bar{\Delta}$ is the normalized change in data transfer values, given as:

$$\bar{\Delta} = \frac{1}{0.5((\max|\phi^n| - \min|\phi^n|) + |\bar{\phi}^n|_{ave})} \Delta \quad (3.17)$$

where

$$\Delta = \frac{1}{\omega} (\phi^n - \phi^{n-1}). \quad (3.18)$$

$|\bar{\phi}^n|_{ave}$ is the absolute value of the mean of all data transfer values at a given iteration. Subscript n and $n - 1$ denote data transfer values from the current and previous iteration, respectively. ω is the under-relaxation factor that is applied.

Here, ω is set to less than 1 for the force transfer (fluid to solid), because under-relaxation does in this case reduce instabilities and oscillatory behaviour of the data

transfers. The under-relaxation algorithm is then given as:

$$\sigma_{relaxed}^n = \sigma^{n-1} + \omega(\sigma^n - \sigma^{n-1}), \quad (3.19)$$

where σ are the forces at the fluid wall transferred and interpolated onto the solid surface. The purpose of under-relaxation is to reduce instabilities by changing the under-relaxed value less rapidly from one iteration to another.

In Fig. 3.3, four convergence criteria are required for the convergence of one coupling step. Criterion 1 is that the flow within Ansys Fluent [5] is converged, as described in Subsection 3.2.2. Criterion 2 and 4 is that the RMS convergence criteria are met for each data transfer. The data transfer values, ϕ , in Eq. 3.16 are the forces at the fluid wall, σ_f , and the wall displacements of the solid, d_s , for data transfer 1 and 2, respectively. Criterion 3 is that the solid in Ansys Mechanical [8] has converged.

Note that a maximum number of coupling iterations within each coupling step are set. Therefore, it is crucial to check the different criteria and their convergence at the end of the simulation. The simulation can move on to the next coupling step even if the four convergence criteria are not met within an iteration. The simulation can be considered successful and completed by the software without the final coupling step being converged.

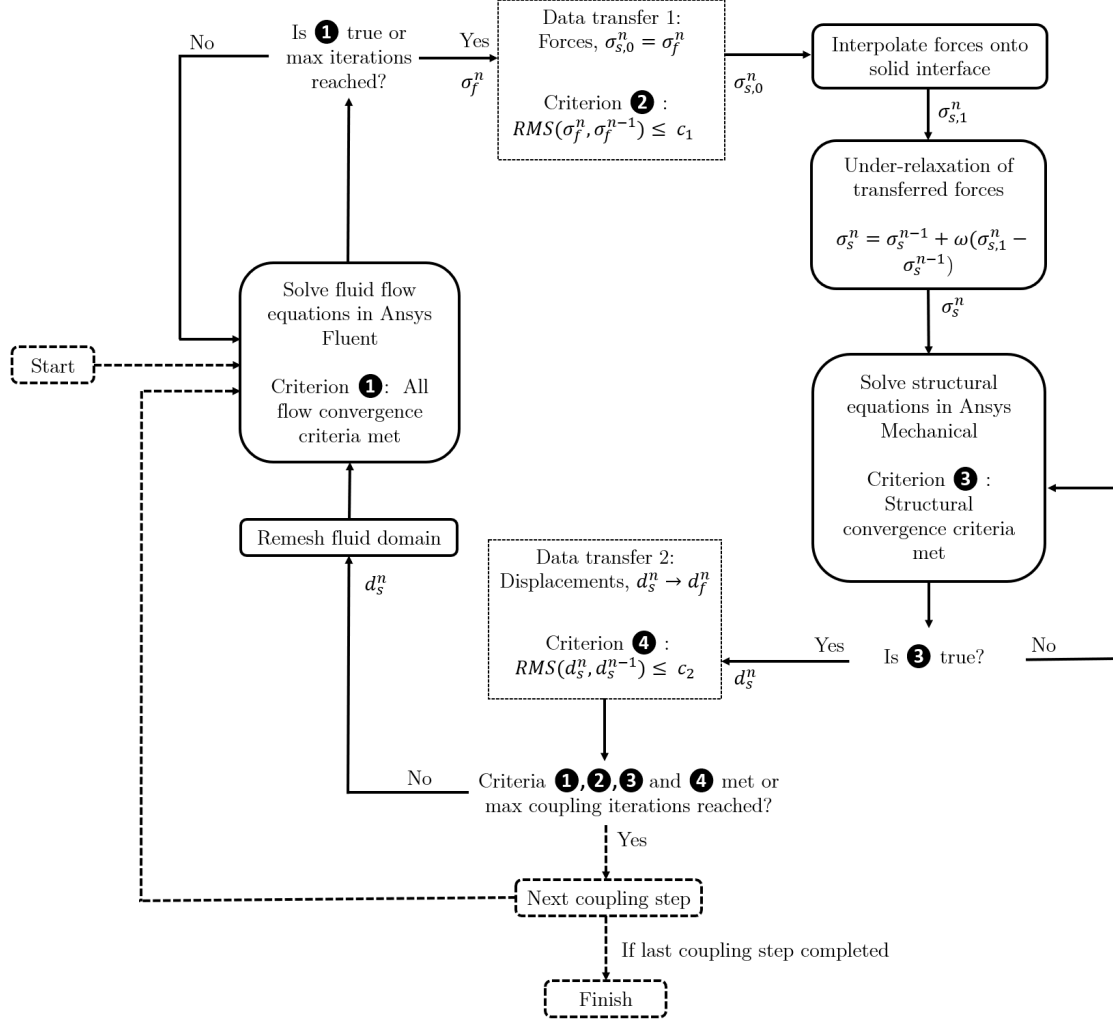


Figure 3.3: Overview of FSI coupling scheme, where n is the current coupling iteration and c_1 and c_2 are the RMS convergence criteria for the data transfers. Flow chart created based on information given in Ansys System Coupling Users Guide [11].

Chapter 4

Simulation Setup

4.1 Problem statement

The problem setup is based on the setups described in Huang [33], Marzo et al. [45] and Hazel and Heil [30] by use of their non-dimensional parameters. The three-dimensional collapsible tube system is shown in Fig. 4.1. As indicated by the difference in shading, the solid tube is divided into three parts. The middle part is flexible, while the parts up and downstream of it are rigid. Fluid flows through the tube with an inner radius of R and wall thickness h . The flexible part of the tube is an isotropic linear elastic material with Young's modulus, E , and Poisson ratio, ν . The upstream rigid part length is $L_{up} = R$, while the two other parts are of length $L_{flex} = L_{down} = 10R$. Boundary conditions and applied forces are presented in the list below.

1. For the structure:
 - (a) Fixed support at both ends of collapsible tube.
 - (b) External uniform pressure on tube wall, p_{ext} , acts normally to the surface.
 - (c) External perturbation load on tube wall, $p_{pert} = a + bx^2$, where $a = p_{ext}/100$ and $b = a/(R+h)^2$ are constants, and x is the coordinate presented in Fig. 4.1.
2. For the fluid:
 - (a) No-slip at the tube wall.
 - (b) Hagen-Poiseuille velocity profile at inlet, $w_{inlet} = 2W_0(1 - (x^2 + y^2)/R^2)$, where W_0 is the average velocity at the inlet.
 - (c) Pressure at outlet, $p_{outlet} = 0$.

The total externally applied pressure on the tube is therefore $p_{tot} = p_{ext} + p_{pert}$. The perturbation load is gradually decreased to 0 through the simulation, as its purpose is to make sure the tube undergoes a two-lobe buckling. How this load is applied is described in Subsection 4.2.1.

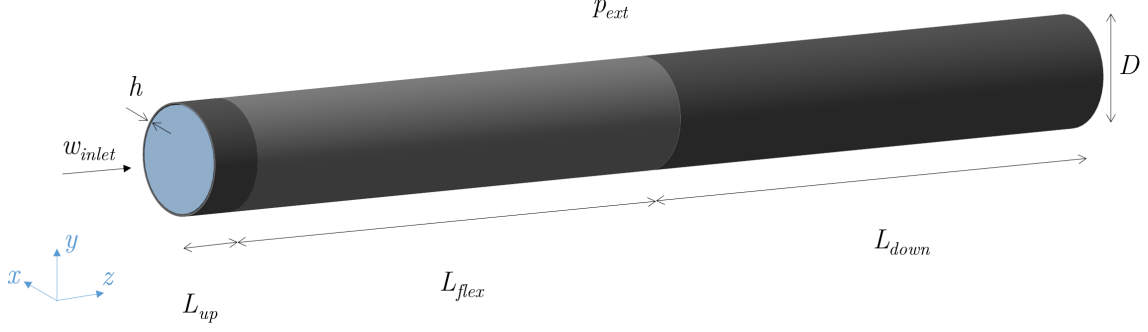


Figure 4.1: Problem geometry schematic. See text for symbol descriptions.

4.2 Main case simulation

Ansys Workbench 2021R2 [12], a platform where Ansys software can be connected, was used for all simulations. Within Ansys Workbench [12], Ansys Spaceclaim 2021R2 [10] was used for geometry creation, Ansys Mechanical 2021R2 [8] for solving structural equations, Ansys Meshing 2021R2 [9] for fluid meshing, Ansys Fluent 2021R2 [5] for solving flow equations and Ansys System Coupling 2021R2 [11] for coupling the fluid and structure. The corresponding systems set up in Ansys Workbench [12] for the mentioned software are Geometry, Transient Structural, Fluid Flow (Fluent) and System Coupling.

Simulations were done on a computer with 32 GB RAM and eight cores, of which seven cores were designated for the simulations. The clock rate of the processors was 1.40 GHz. Results were post-processed in Ansys CFD-post [3] and MATLAB R2021a [46].

For the main case (or verification case) simulation, all parameters and geometries are chosen per the non-dimensional parameters given in Huang [33]. This section includes the non-dimensional and the derived dimensional parameters. In addition, grid generation and necessary software settings and applied loads will be explained. However, a complete guide for setting up the model can be found in Appendix A for the reader to see all details or recreate the model.

Huang [33] presents four non-dimensional numbers to describe the collapsible tube system; Mass ratio M , Reynolds number Re_0 , bending stiffness K_b and non-dimensional downstream transmural pressure P_e , given by the following relations with corresponding values:

$$\begin{aligned} M &= \frac{\rho_m h}{\rho D} = 25, & Re_0 &= \frac{U_0 D}{\mu} = 128, \\ K_b &= \frac{E h^3}{12(1 - \nu_s^2) \rho U_0^2 D^3} = 0.030517, & P_e &= \frac{p_e - p_0}{\rho U_0^2} = 5.46875, \end{aligned} \quad (4.1)$$

where the explanations for each variable are given in Table 4.1 with corresponding dimensional values in the rightmost column.

Table 4.1: Parameters used in the main simulation, with units and dimensional values.

Variable		Unit	Value
ρ_m	Density of solid	kg/m^3	1000
ρ	Density of fluid	kg/m^3	1
h	Thickness of tube wall	m	0.025
D	Inner diameter of tube	m	1
U_0	Average inlet velocity	m/s	0.506
E	Youngs modulus of solid	Pa	3559.4
ν_s	Poisson ratio of solid	—	0.49
μ_s	Dynamic viscosity of fluid	—	$3.95 \cdot 10^{-3}$
ρ	Density of fluid	kg/m^3	1
p_e	Applied pressure on solid	Pa	1.4
p_0	Pressure at fluid outlet	Pa	0
a	Perturbation load constant ($p_{ext}/100$)	Pa	$1.4 \cdot 10^{-2}$
b	Perturbation load constant ($a/(R + h)^2$)	Pa/m^2	$5.08 \cdot 10^{-2}$

The formula for the perturbation load constant, b , is as given in Huang [33], while a is 10 times larger in Huang [33]. A smaller magnitude load is applied here because it proved to be sufficient to obtain 2-lobe buckling, and using a smaller load made the first coupling steps of the simulation reach convergence faster.

4.2.1 Solid parameters

Solid mesh

The solid tube is modelled as a membrane with bending and therefore consists of shell elements, with one element in the thickness of the tube. The mesh consists of 1600 quadratic hexahedral shell elements. Quadratic element order is chosen, meaning there are nodes on element corners and on mid sides. In addition, the function called straight-sided elements is turned off, meaning that the nodes on the element sides will be placed in such a way to best capture the shape of the geometry. Note that only the flexible part of the tube is modelled and meshed because the two other parts are rigid and at rest.

In order to determine how fine the mesh needs to be, a grid refinement study was done by modelling the structure without flow through while exposed to externally applied pressure (perturbation load and high enough pressure for the tube to get close to collapse) with different element sizes. Figure 4.2 displays the maximum deformation obtained across the tube with decreasing element size. Maximum deformation is used to evaluate mesh independence in this case because the deformation of the solid is the most important factor which affects the fluid and hence the entire FSI system. As can be seen, the value for the maximum deformation is independent of element sizes below 0.2 m. However, the element size used is set to 0.1 m because other values, such as maximum equivalent elastic strain, changed significantly when reducing the element size from 0.2 to 0.1 m.

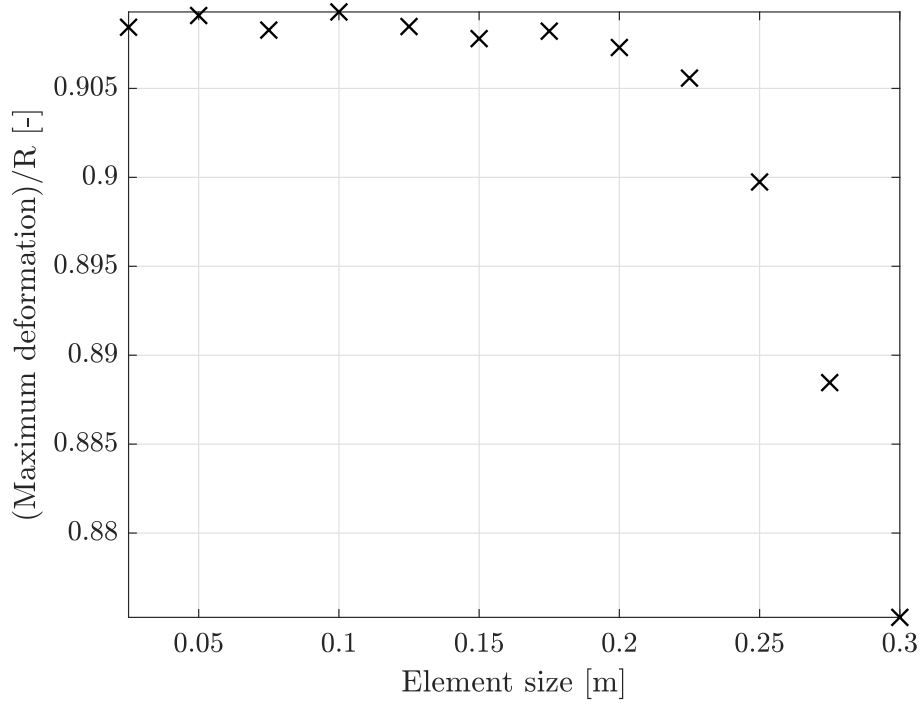


Figure 4.2: Maximum deformation obtained for the solid tube with different element sizes of the mesh. Final external pressure exposure on the tube, in this case, is 0.3 Pa.

Applied Loads and Step Size

The uniform load is increased gradually until the value of p_{ext} is reached, while the perturbation load is gradually reduced to 0. This is done by setting the *End Time* of the simulation to 1s and applying the following loads:

$$p_{ext}(time) = p_{ext} \cdot time \quad (4.2)$$

$$p_{pert}(x, time) = (a - bx^2)(End\ Time - time) \quad (4.3)$$

Note that even though time is included in these expressions, time integration is turned off in the simulations, meaning that transient effects are not included. The software solves a steady problem for the increased external load for each step. The step size is adaptive and in the range of 0.1 s to 10^{-8} s. This means that Ansys Mechanical [8] adjusts the step size based on the analysis conditions of the simulation so far [7](Ch. 14.5). Note that the end time within Ansys Mechanical [8] and in the coupling scheme is the same. However, the time stepping is not necessarily the same. One coupling step can, for instance, be 0.1 s. Within each iteration of that coupling step, the solid can go through multiple time steps (or static load steps).

Fixed support is added on the edges of the tube surface and the surface is given a fluid-structure interface property to later be connected in Ansys System Coupling [11].

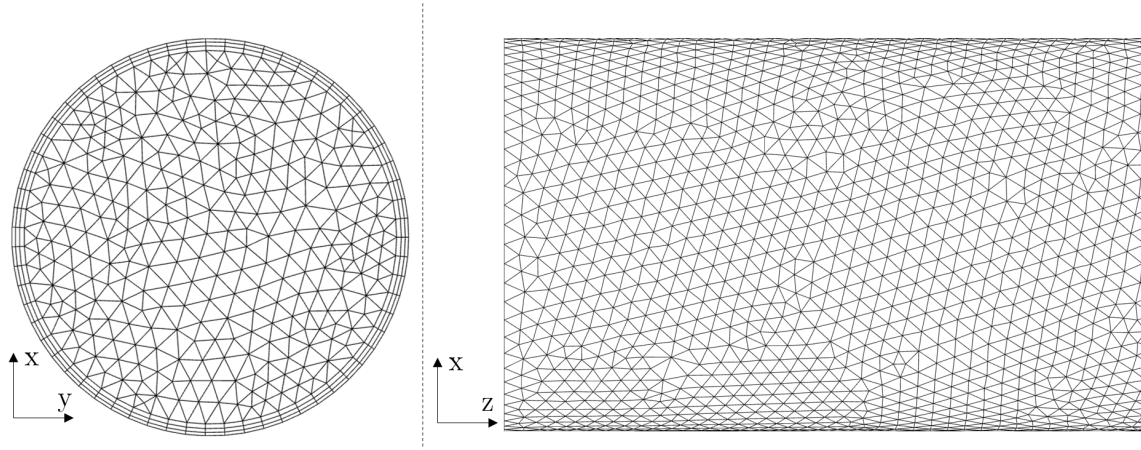


Figure 4.3: Fluid mesh from two views: Fluid flow inlet (left) and part of fluid wall (right). Images used courtesy of ANSYS, Inc.

4.2.2 Fluid parameters

Fluid Mesh

The fluid mesh consists of approximately 314 000 tetrahedral cells. Tetrahedral cells are used because the dynamic mesh and remeshing work better with tetrahedrons than with other types of cells. The element order is, as for the solid mesh, quadratic. A small inflation layer with three layers and an aspect ratio of 0.25 is applied near the wall. Without it, remeshing does not work properly when deformations become large. Figure 4.3 displays the mesh from two different views.

A mesh independence study on the fluid domain for the tube without deformation revealed that an element size of $D/20 = 0.05m$ was sufficient. The mesh independence was evaluated by investigating the grid convergence index (GCI) according to the policy of the Journal of Fluids Engineering [19]. Three mesh sizes were considered and three flow parameters were compared, all presented in Table 4.2. In the table, h , N , and r are the element sizes, the total number of elements in the mesh and the element size ratio, respectively. For example, $r_{21} = h_2/h_1$. The numbers denote which mesh the value is related to, where 1 is the most refined mesh, 2 is the medium mesh (also the one used in the simulations) and 3 is the coarsest mesh. Comparing the medium mesh with the most refined mesh gave a GCI value between 1.4 % and 1.65 % for the two compared values. Pressure at two points along the tube is chosen as comparing values because the pressure distribution along the tube is of high importance in the fluid-structure interaction case. The GCI values are considered to be sufficiently low.

Dynamic mesh

The fluid domain experiences severe deformations during the simulation and the dynamic mesh option in Ansys Fluent [5] must therefore be enabled. The methods used to change the mesh are smoothing, which adjusts the mesh by moving

Table 4.2: Overview of Grid Convergence Index (GCI) study for the fluid mesh.

	$\phi = \text{pressure at}$ $(x,y,z)=(0,0,0)$	$\phi = \text{pressure at}$ $(x,y,z)=(0,0,5)$
h_1, h_2, h_3	0.0333, 0.05, 0.075	
N_1, N_2, N_3	807863, 313717, 118247	
r_{21}, r_{32}	1.5, 1.5	
ϕ_1	0.68	0.358
ϕ_2	0.683	0.36
ϕ_3	0.687	0.363
GCI_{fine}^{21}	1.65%	1.40%
GCI_{coarse}^{32}	2.18%	2.07%

nodes (number of nodes and their connectivity remain unchanged [5](Ch. 11.6.2.1) and remeshing, which regenerates the mesh when deformations become large. A diffusion-based smoothing and a unified remeshing are chosen. In addition, the mesh size must be retained so the cells do not become too small and distorted when deformations become large. Combining smoothing and remeshing is advantageous because smoothing can be used alone when deformations are small, while remeshing is applied locally when cells are too distorted. In this case, the remeshing criteria are based on maximum skewness. If maximum cell skewness exceeds 0.8 or maximum face skewness (cells adjacent to the fluid-structure interface) exceeds 0.7, the cells will be remeshed.

The fluid wall in contact with the flexible part of the solid is assigned a dynamic mesh zone with system coupling property, later connected to the solid wall in system coupling.

Boundary conditions

The boundary conditions for the fluid are applied as described in section 4.1.

4.2.3 System Coupling Parameters

The under-relaxation factor for the data transfer from the fluid to the solid, ω , is set to 0.3, giving stable data transfers without oscillations.

Until half the time has been reached, i.e., when half of the external load has been applied (when $time = 0.5$ s), the deformation remains small, and therefore a large time step of 0.1 s is used. After this point, the time step is reduced to 0.01 s because the tube buckling has become sufficiently large and the tube deforms faster with increased pressure. Although a larger time step could likely be used between certain time steps of the simulation, the time step is held at 0.01 s from 0.5 s to 1 s for convenience, as Ansys System Coupling [12] does not allow for predefining varying time steps. This means that if the time step size is to be changed, the simulation

must be stopped manually and started again with the new time step.

4.3 Simulations with increased Reynolds numbers

In addition to the main simulation, the effect of increasing the Reynolds number was also investigated. The increased Reynolds number cases had $Re_2 = 2 \cdot Re_0$ and $Re_5 = 5 \cdot Re_0$, respectively. From now, when considering the comparison of the different Reynolds number cases, they will be referred to by the following names: Re_0 -case, Re_2 -case, and Re_5 -case.

The Reynolds number was increased by increasing the inlet velocity, which resulted in higher pressure in the flow. Therefore, the tube's external pressure was also increased to deform towards collapse. If the external pressures in the higher Reynolds number cases were of the same magnitude as in the main case simulation, the tube would not deform much. Both the uniform and the perturbation pressure in Eq. 4.2 and 4.3 were increased proportionally to the Reynolds number, i.e., $End\ Time = 2$ s for the Re_2 -case.

Chapter 5

Results and discussion

5.1 Main case: Results and discussion

5.1.1 Comparison of results with previous numerical research

A comparison of results obtained in this study and the ones obtained by Hazel and Heil [30], Huang [33], and Marzo et al. [45] can be seen in Figure 5.1 and 5.2, where the non-dimensional pressure along the entire tube centerline (at $x = 0, y = 0$) and the wall shape of the flexible part of the tube, respectively, are plotted. The figures show that great agreement is obtained with the results by Hazel and Heil [30], Huang [33], and Marzo et al. [45]. The values from the literature are obtained from reading image plots, leading to errors that are hard to quantify. One quite clear difference is that the deformations in the y-z-plane are slightly larger in the most deformed part. There can be many reasons for these deviations, such as differences in how each solver's governing equations are solved, too coarse mesh, or inaccuracy in data transfers. The two latter potential causes have been investigated by executing a mesh independence study for the entire system and running the simulation with different convergence criteria for the data transfers. Results are shown in Subsection 5.2.

5.1.2 Qualitative comparison of results with experiments

Experiments with similar non-dimensional parameters have not been conducted, and quantitative comparison with experiments will not be made. However, an indication of whether the phenomena occurring in the simulations are physical can still be discussed by comparison with other experiments.

The first aspect that will be addressed is the location of the largest displacement. As mentioned in Chapter 2, experiments show that the most deformed part of the tube is closer to the downstream end of the flexible part than the upstream end because of friction losses through the tube. This is also the case for the simulation in this study, as can be seen in Fig. 5.3.

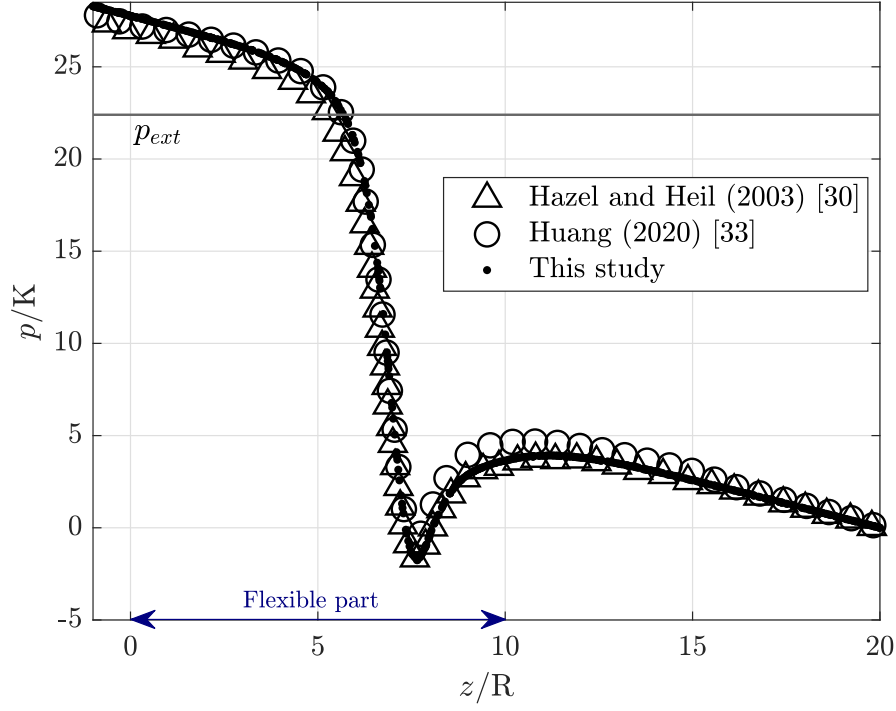


Figure 5.1: Pressure along the centerline of the tube. Pressure and length down the tube are non-dimensionalized by dividing it by the flexural rigidity, $K = \frac{Eh^3}{12R^3(1-\nu^2)}$ and the undeformed radius, R , respectively. Note that $z/R = 0$ indicates where the flexible tube part begins and $z/R = 10$ is the flexible tube part's end. The horizontal line indicates the externally applied pressure, p_{ext} .

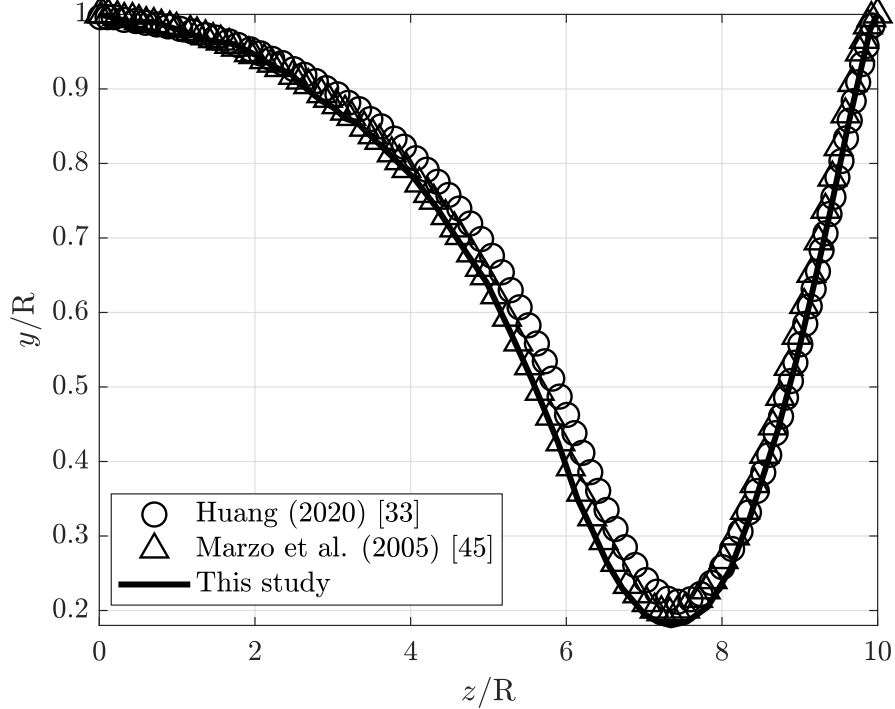


Figure 5.2: The shape of one side of the tube wall (flexible part only) in the y - z -plane. Due to the symmetry, in this case, the shape is similar on the other tube wall side, and the shape of one side only is plotted. Both length scales are non-dimensionalized by the radius, R .

In addition, it can be observed (see top contour plot in Fig. 5.11) that there is a reverse flow in a small area downstream of the most deformed part, as also observed in the experiments of Bertram and Godbole [16]. Reverse flow will be discussed further in Section 5.3.

Bertram and Godbole [16] did experiments on flow through a rigid tube with a 2-lobe-shaped throat and observed parallel velocity jets, similar to the ones seen in the x-z-plane of this study, see bottom contour plot of Fig. 5.5.



Figure 5.3: Deformation of the flexible part of the tube from two views. Images used courtesy of ANSYS, Inc.

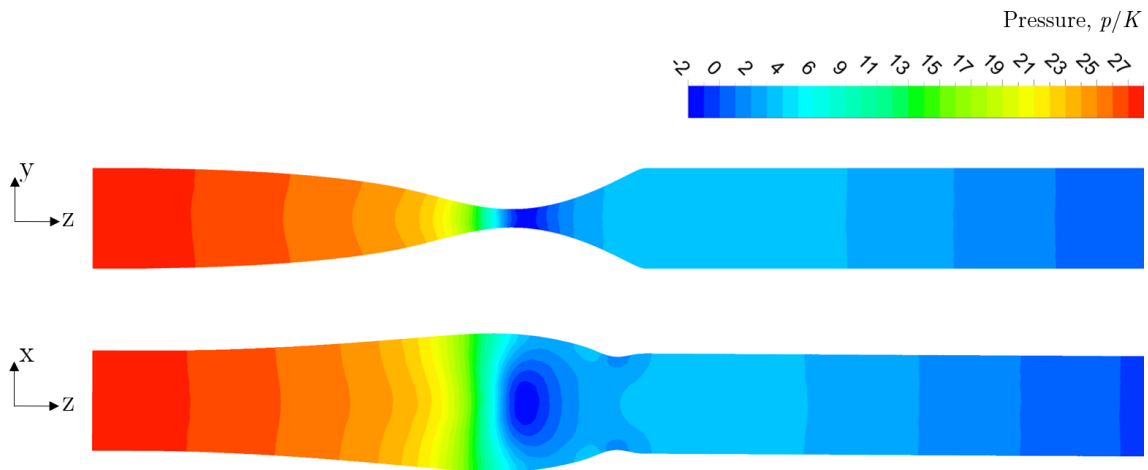


Figure 5.4: Pressure contour plots of flow in the y-z-plane (top) and the x-z-plane (bottom). Images used courtesy of ANSYS, Inc.

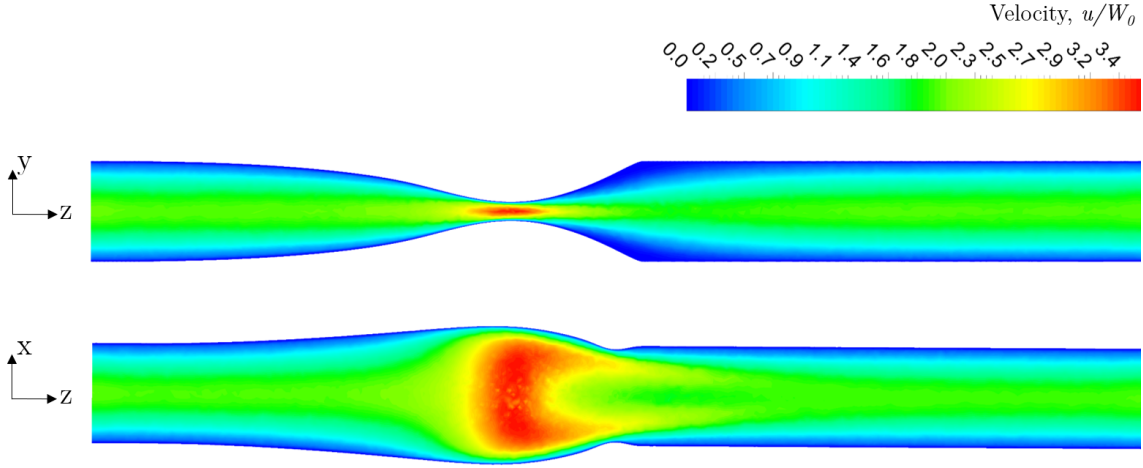


Figure 5.5: Velocity contour plots of flow in the y-z-plane (top) and the x-z-plane (bottom). Images used courtesy of ANSYS, Inc.

5.1.3 Velocity and pressure distribution

While Fig. 5.1 gives a good indication of the pressure distribution along the tube, it fails to show some phenomena. In Fig. 5.4 it can be observed that in addition to the lowest pressure areas in the most collapsed part of the tube, two low-pressure areas can also be observed at the edge where the flexible part meets the downstream rigid part. This has also been observed by Hazel and Heil [30] and Huang [33]. The reduced pressure leads to a minor buckling of the wall in the opposite direction of the main buckling (most collapsed tube part), which can be seen as the small dimple in the top image of Fig. 5.3. This buckling occurs because the compressive load at the downstream end of the flexible tube is large [30].

Evaluation of using a laminar flow model

The largest velocity obtained in the smallest cross-section is 1.8 times larger than the maximum inlet velocity, i.e., 3.6 times larger than the average inlet velocity. Even though the Reynolds number of the flow at the inlet, $Re = 128$, is within the laminar range, $Re < 2000$, for flow in straight cylindrical tubes, it is interesting to evaluate the Reynolds number in different cross-sections.

The Reynolds numbers, $Re = D_h U_{avg}/\nu$, were calculated with reference to the hydraulic diameter, $D_h = 4A/P$, where A is the cross section area and P is the perimeter. A total of 6 cross sections within the deformed tube part were looked into and showed that the Reynolds number stayed in the range of 127 to 129, meaning that it is well within the range of laminar flow in cylindrical tubes.

However, whether the flow is turbulent, in transition, or laminar can not be determined solely based on the Reynolds number (as for steady flow through straight constant-diameter pipes) when the fluid flows through a constriction [70], as is the case for the collapsible tube. In these cases, the geometry of the constriction is also of importance [70]. Therefore, to determine the effect of using a laminar flow

model, the same simulation was run with the $k - \omega$ SST turbulence model. The results deviated by 0.6% in maximum tube deformation from the simulation with the laminar flow. The pressure curve along the centerline of the tube was almost identical, with the largest deviation at the inlet with a 1% difference and decreasing deviation downstream of the inlet. The effect of using a turbulence model, in this case, is therefore small, and using a laminar model to verify the model and observe the pressure drop and tube deformations is justified.

5.2 Main case: Effects of changing simulation set-up

5.2.1 Mesh refinement study of the coupled system

In addition to doing a mesh refinement study on each domain, a mesh refinement study was also done for the coupled system. See Table 5.1 for details on the meshes tested and their respective total CPU run times. Figure 5.6 shows the comparison of the pressure along the tube centerline for the three cases. The simulation with the coarsest mesh, Case A, resulted in relatively large deviations from Case B compared to those between Case B and C. The close-to-identical results of Cases B and C indicate that the meshes in Case B are sufficiently fine.

When the solid element size is halved, the number of nodes and elements is multiplied by 4. For the fluid mesh, the shape of the domain makes this factor larger, and it is closer to 5.

The time spent by Ansys System Coupling [11] was 4 minutes for all three cases. This can indicate that time spent transferring data is less dependent on how much data is transferred (number of transfer points) but more on how often it is transferred. In these cases, the coupling step sizes were identical, and the total amount of iterations performed were 518, 529, and 533 for Case A, B, and C, respectively. The amount of time spent by Ansys Fluent [5] relatively to Ansys Mechanical [8] increased from 69% to 80% from Case A to C. This implies that reducing the element size for the fluid and solid with the same factor increases computational time for the fluid more than for the solid. One potential reason for this could be because the amount of elements for the fluid is increased by a factor of approximately 5, rather than 4, as for the solid, when the element size is halved. It is also possible that the dynamic meshing of the fluid domain is responsible for the difference, as the domain might have to remesh more often due to the fact that smaller cells will become more distorted than larger cells if the same deformation is applied. Hence, in cases where the coarser mesh only needs smoothing to deform into the desired domain shape, the finer mesh might need remeshing.

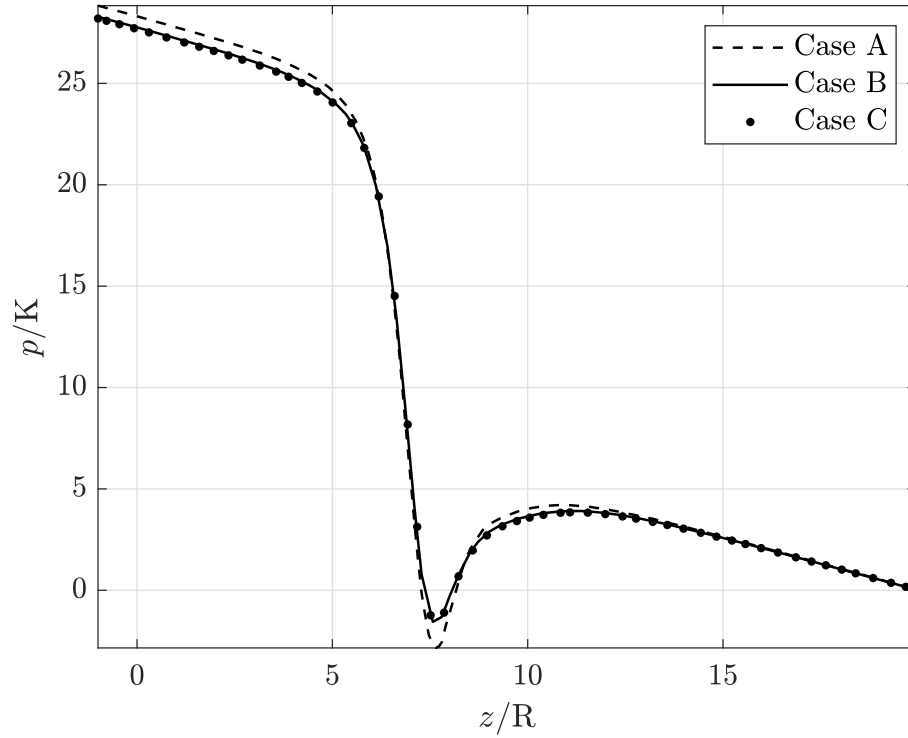


Figure 5.6: Pressure at tube centerline for simulations with three different mesh sizes. See Table 5.1 for mesh details.

Table 5.1: Details of mesh sizes used and total computational time spent for the simulations in the mesh refinement study of the coupled problem.

Case	Solid domain element size [m]	Fluid domain cell size [m]	Total CPU run time
A	0.2	0.1	1 hour 21 minutes
B	0.1	0.05	4 hours 24 minutes
C	0.05	0.025	20 hours 11 minutes

Fluid mesh quality

Cell skewness and orthogonal quality are commonly used metrics to evaluate the quality of meshes. Values of both metrics are in the range of 0 to 1. High values for orthogonal quality and low values for skewness are recommended. Since the fluid mesh is automatically changed by Ansys Fluent [5] through the Dynamic Mesh functionality throughout the simulation, the mesh is evaluated before and after running the simulation.

The cosine of the angle between the normal face vector (vector from cell center to the center of each adjacent cell) and the vector from cell center to each cell face is calculated for all cell faces. The smallest value of all the cosine values within one cell becomes the cell's orthogonal quality [9](p. 142).

Figure 5.7 displays the distribution of cells in terms of orthogonal quality for the fluid mesh in its initial cylindrical shape and the final deformed state (at simulation end). The orthogonal quality is slightly reduced from the initial to deformed state. However, there are few elements of low quality, and none under the Ansys Meshing [9] minimum recommendation of 0.1.

Cell equivolume skewness for a cell is calculated by dividing the difference between the optimal cell size and the cell size, by the optimal cell size. The optimal cell size of a cell is the size of an equilateral cell with the same circumradius. A perfectly equilateral cell, therefore, has a skewness value of 0. Low values for skewness are wanted because the solver assumes that the cells are relatively equilateral [9](p. 140).

Cell equivolume skewness is slightly higher for some cells in the deformed mesh. Regardless, the values here are also acceptable, with 96% of the cells with less than 0.5 in skewness for the deformed mesh. The corresponding value for the initial mesh is 99%. The maximum values are 0.72 and 0.79 for the initial and deformed mesh. The maximum allowed cell skewness was automatically set to 0.8 in the Dynamic Mesh function of Ansys Fluent [5] and the requirement is held. In the Ansys Meshing Users Guide [9](p. 140), cell quality is considered to be good when skewness is below 0.5, fair between 0.5 and 0.75, poor between 0.75 and 0.9, and bad above 0.9. Reducing the maximum skewness limit could be considered to ensure no cells have higher skewness than 0.75. However, in this case, there are few cells in the poor quality range, and reducing the limit could require higher computational efforts. See Fig. 5.8 for skewness distribution for the initial and final deformed fluid mesh.

The poorest quality cells are developed close to where the tube deforms the most, both on the boundary and for cells adjacent to it, which is reasonable as the largest domain changes occur in that area.

In this case, the mesh quality is considered good enough, and the dynamic mesh functionality of Ansys Fluent [5] works well. However, the mesh quality can worsen where deformations are large. Although the Dynamic Mesh functionality of Ansys

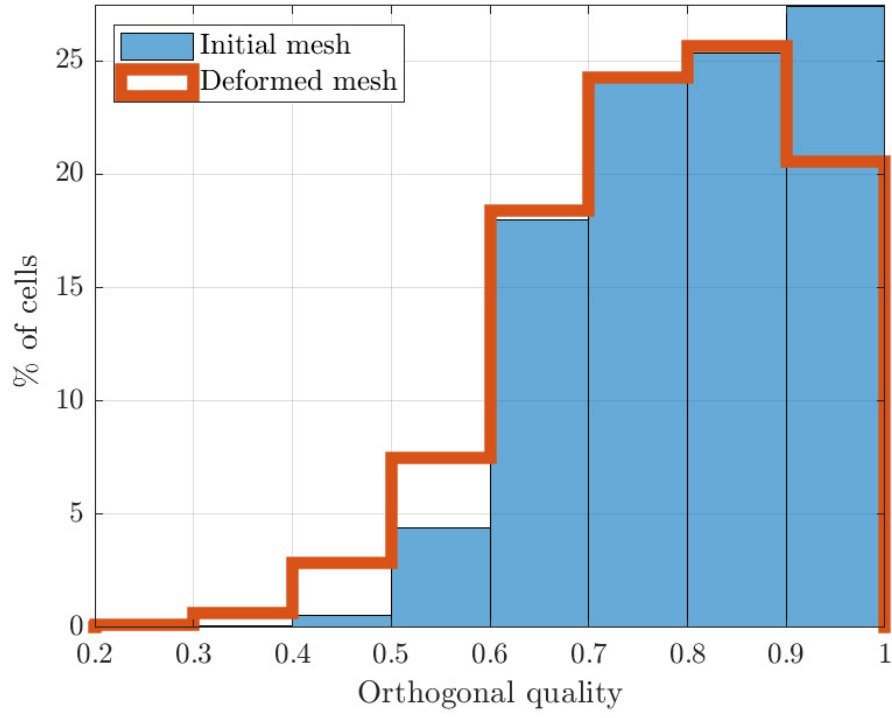


Figure 5.7: Orthogonal mesh quality distribution of the initial and final deformed fluid mesh, respectively.

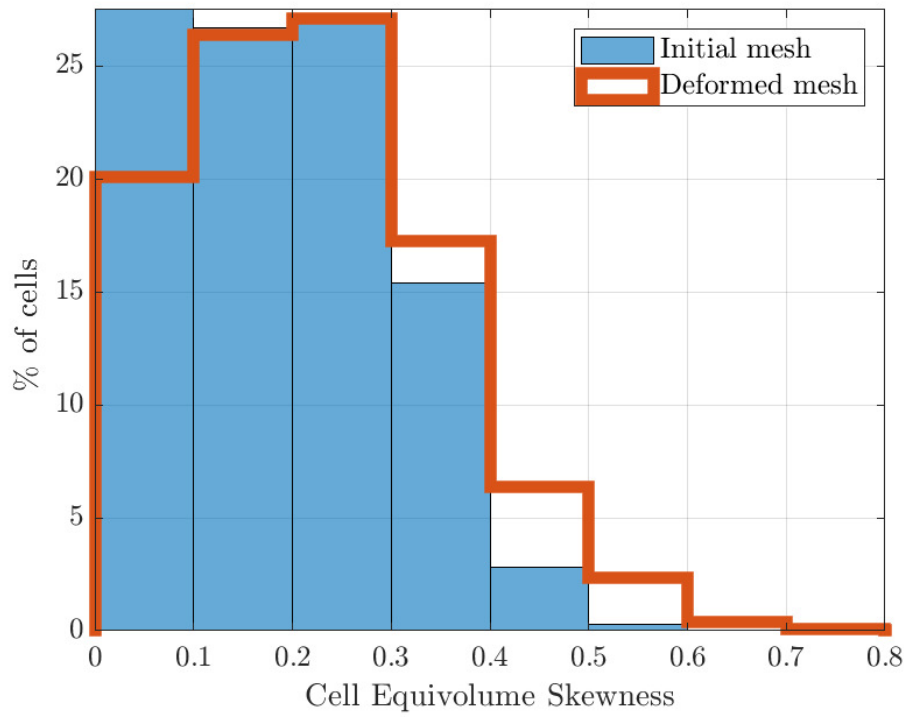


Figure 5.8: Cell equivolume skewness distribution of the initial and final deformed fluid mesh, respectively.

Fluent [5] can keep the cell skewness below the criteria as the domain changes, the mesh should be monitored to ensure that there are only a few cells of poor quality in the final deformed mesh.

Since opposite tube walls do not get in contact in this case and there is still some distance between them in the most deformed part, retaining the size distribution works. However, for future cases, if the goal is to get closer to collapse, these settings might have to change to ensure that unreasonably few cells in the thickness of the fluid domain are not obtained. Therefore, allowing for smaller cells in the collapsing part could be beneficial.

5.2.2 Data transfer convergence

Data transfer convergence and stability

Two of the main bottlenecks before the first successful simulation were unstable data transfers (RMS-values increased and decreased alternately between coupling iterations within the same coupling step) and difficulties with remeshing the fluid domain. Applying under-relaxation to the force data transfer and retaining the mesh size distribution in Ansys Fluent [5] helped overcome these issues. This resulted in stable data transfers, where the data transfer RMS-values decreased with each iteration within each coupling step. Between 5 and 16 iterations were necessary within each coupling step to reach the RMS convergence criteria of 0.01.

For future work, applying other stabilization techniques in addition or instead of under-relaxation should be considered to investigate their effect on convergence and simulation efficiency. The other techniques available in Ansys System Coupling [11] are ramping and quasi-Newton stabilization.

In addition to the investigation of new techniques, a structured study of which values of the under-relaxation factor are most optimal would be beneficial to conduct. The under-relaxation factor used in these simulations was chosen based on trial and error. Large factors were first tested and were gradually reduced until the simulation could successfully run without crashing. The value of 0.3, used for all simulations, gave stable data transfers without unnecessarily small coupling step sizes or too high computational time. In order to find the optimal under-relaxation factor, it should be investigated with different coupling step sizes because both affect each other and hence the overall computational effort needed.

Effects on changing data transfer convergence criteria

In order to understand the significance of the data transfer convergence, two other convergence criteria were tested. Besides the default criteria of $RMS < 0.01$, additional simulations with $RMS < 0.1$ and $RMS < 0.5$ were run.

The results showed that the differences in the results obtained from the three simulations were very small. The maximum deformations obtained were 0.40989, 0.40973

and 0.40962 for $RMS < 0.5$, $RMS < 0.1$ and $RMS < 0.01$, respectively. This gives a 0.07% difference in maximum deformation from the highest to lowest convergence criteria, which shows that the default RMS criterion is unnecessarily tough for these simulations. The displacement data transfer (from solid to fluid) obtains significantly lower RMS-values than the force data transfer (from fluid to solid). While the force data transfer reaches RMS-values just below the convergence criteria, the displacement data transfer RMS-values are usually 1 to 3 orders of magnitude smaller, which also yields for the higher convergence criteria. This might be why small differences in results are observed for differing criteria, as the tube displacement RMS-values are less than the default RMS criteria in all cases.

The results presented in this and the two previous subsections indicate that the deviations between the results obtained from this study and the verification articles are not likely due to poor mesh or data transfer convergence criteria, given that the models from the verification articles have used sufficiently fine meshes and strict enough convergence criteria. Therefore, differences in approximations of the fluid and solid equations are possibly causing the differences. Changing the convergence criteria within Ansys Fluent [5] from 10^{-5} (The criteria used in the simulations) to 10^{-3} (Ansys Fluent [5] default criteria) gave a difference in fluid inlet pressure of 1.3%. This indicates that relatively small differences in the fluid flow model can change the entire system. As the fluid flow solver defined in Ansys Fluent [5] with the applied settings is built differently than those in the articles, it is reasonable that some deviations appear. Some aspects that can be investigated in future work are the use of different schemes of different orders. Other possible reasons for the deviations could be difference in coupling step size and how the boundary conditions are applied.

5.3 Effects of increasing the Reynolds number

As can be seen from Fig. 5.9, increasing the Reynolds number results in that the lowest pressure point, and the largest deformation, is moved more downstream. This is an expected trend because of the increased pressure drop through the tube and was also observed in the numerical simulations by Hazel and Heil [30].

In addition, a comparison of the Re_0 and Re_2 -cases shows that the area occupied by reverse flow in the y-z-plane, after the most deformed part, is significantly increased in the Re_2 -cases. This happens because the point of largest deformation is more downstream for the higher Reynolds number case, leading to a steeper deformation until the rigid downstream part in the y-z-plane, making the onset of separation happen earlier. See the vector plots in Fig. 5.11.

In the Re_5 -case, the most collapsed part is even more downstream, see Fig. 5.14. However, in this case, a 3-mode buckling appeared. See Fig. 5.12 for differences in buckling patterns with Reynolds number. The Re_5 -case starts to buckle in a 2-lobed shape like the lower Reynolds number cases but shifts as the external pressure increases past a certain point. Figure 5.13 displays this development. It must be emphasized that the difference in the simulation results is not only affected by the

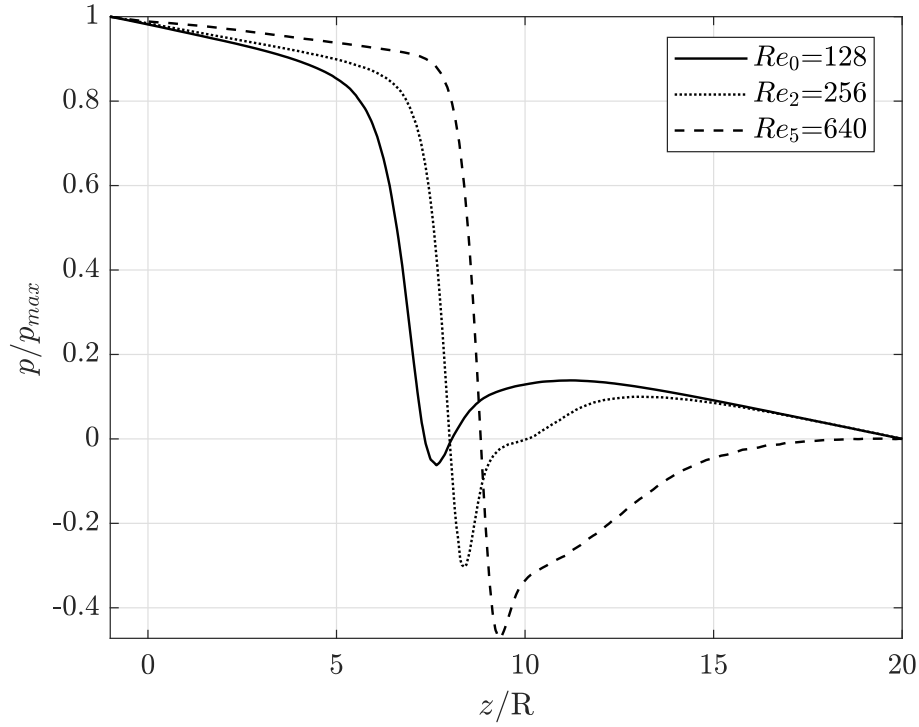


Figure 5.9: Pressure along the tube centerline for the different Reynolds number cases. Note that the pressure has been divided by the maximum pressure (i.e., inlet pressure) of each respective case to compare the curve's shape.

differing Reynolds numbers but also by the applied loads. Here, a linear increase in uniform external pressure and perturbation load with Reynolds number is applied. It is, for instance, possible that the linear increase in pressure is too large and that a smaller increase would be more appropriate. A more fruitful comparison of the effect of the Reynolds number might arise if the external pressure is instead held constant while changing the Reynolds number by changing the pressure at the inlet (not having a velocity-driven inlet) while keeping the downstream pressure constant. However, since the shift to a 3-mode buckling happens before $time = 2$ s, the external pressure is not larger than that of the Re_2 -case. It is, in fact, lower, and the perturbation load is larger than that of the Re_2 -case. This indicates that the higher Reynolds number flows are more prone to achieve 3-lobe buckling than when Reynolds numbers are lower.

Zhu et al. [73] showed that the shorter a tube is and the thicker its walls are, the more prone it is to higher mode buckling. As shown in Fig. 5.10, the transmural pressure for the Re_5 -case is negative closer to the flexible tube end than in the lower Reynolds number cases. This can perhaps explain why the highest Reynolds number case gave three mode buckling; the deformation is now concentrated to a smaller part of the tube, so the tube can be viewed as a shorter tube in the sense of collapsing.

It can also be observed that the cross-sectional shape of the tube in the Re_2 and Re_0 -cases differ, see Fig. 5.12. What this difference is caused by will not be discussed further because in order to do a more detailed analysis of the flow fields and buckling shapes for the higher Reynolds number cases, a thorough mesh refinement study

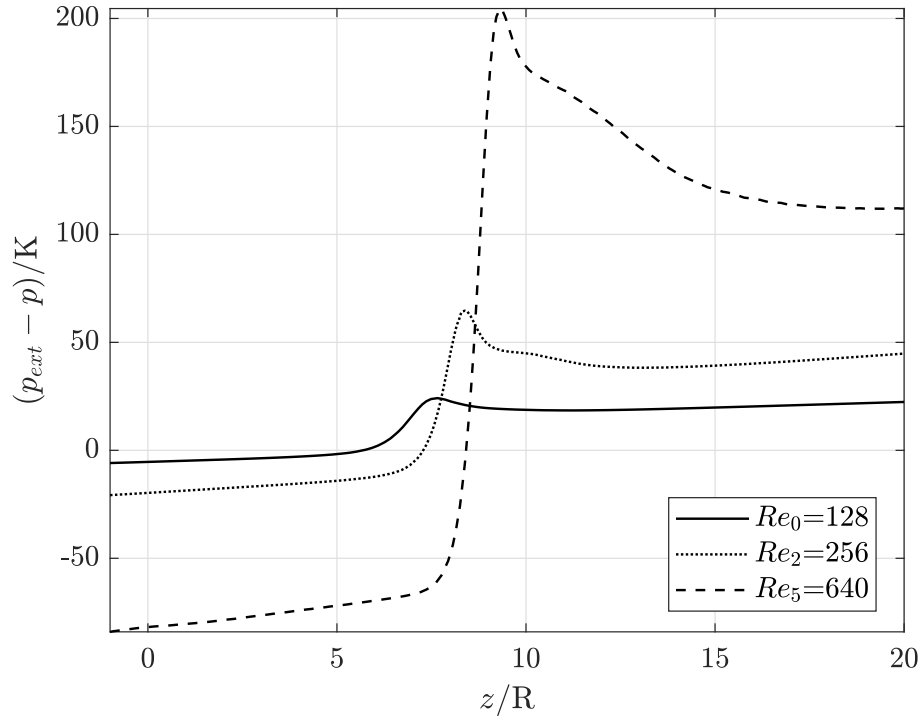


Figure 5.10: Pressure difference between the externally applied pressure and the pressure at flow centerline for the different Reynolds number cases.

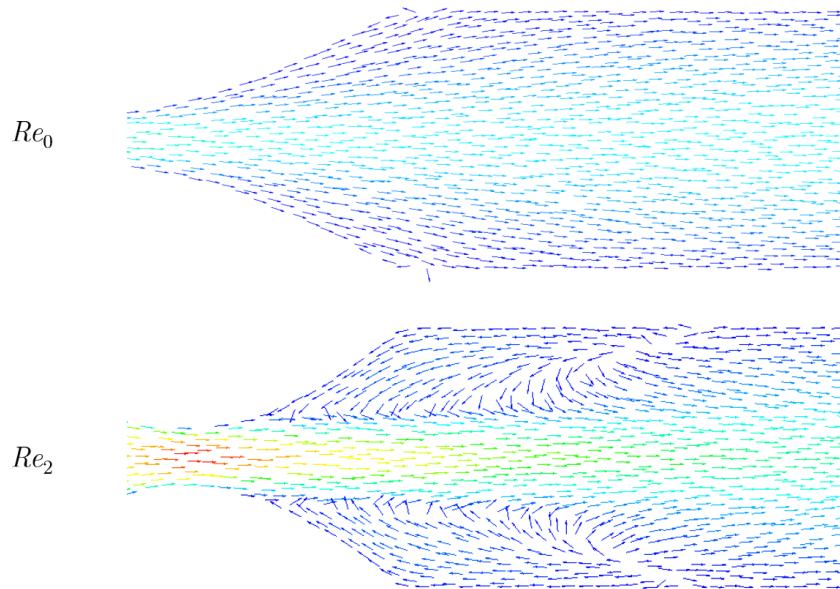


Figure 5.11: Velocity vectors in a part of the y-z-plane (where the flexible part meets the downstream rigid part). The length of the vectors are normalized. The colours indicate the velocity magnitude with similar qualitative color-scaling as in Fig. 5.5. Images used courtesy of ANSYS, Inc.

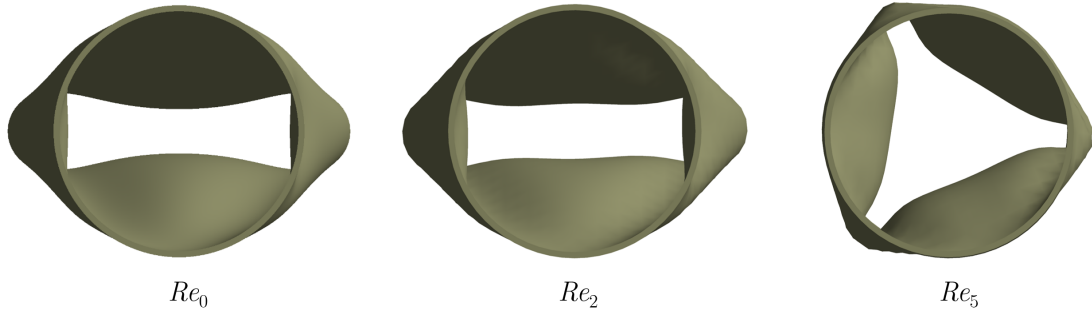


Figure 5.12: Cross sectional views of the final tube configuration for the different Reynolds number cases. Images used courtesy of ANSYS, Inc.

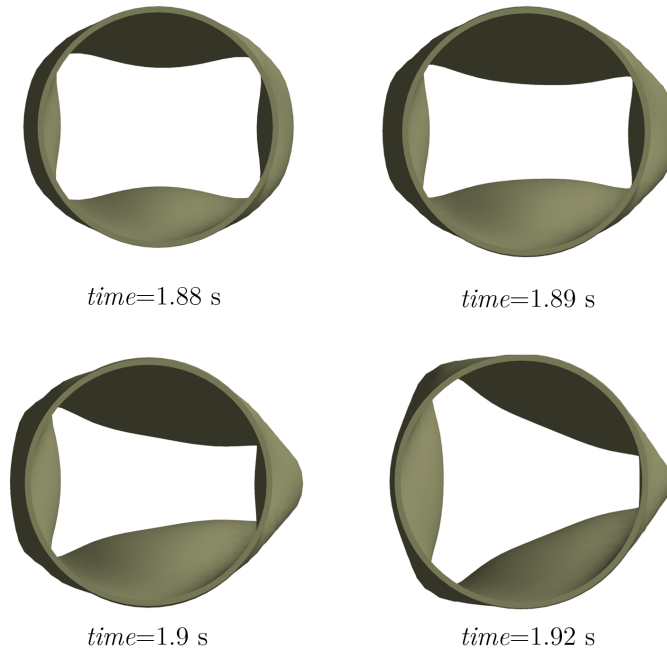


Figure 5.13: Development of the buckling pattern through some time steps of the Re_5 -case. $time$ is representing the external loads applied to the tube. Insert the $time$ into Eq. 4.2 and 4.3 to find the externally applied loads. Images used courtesy of ANSYS, Inc.

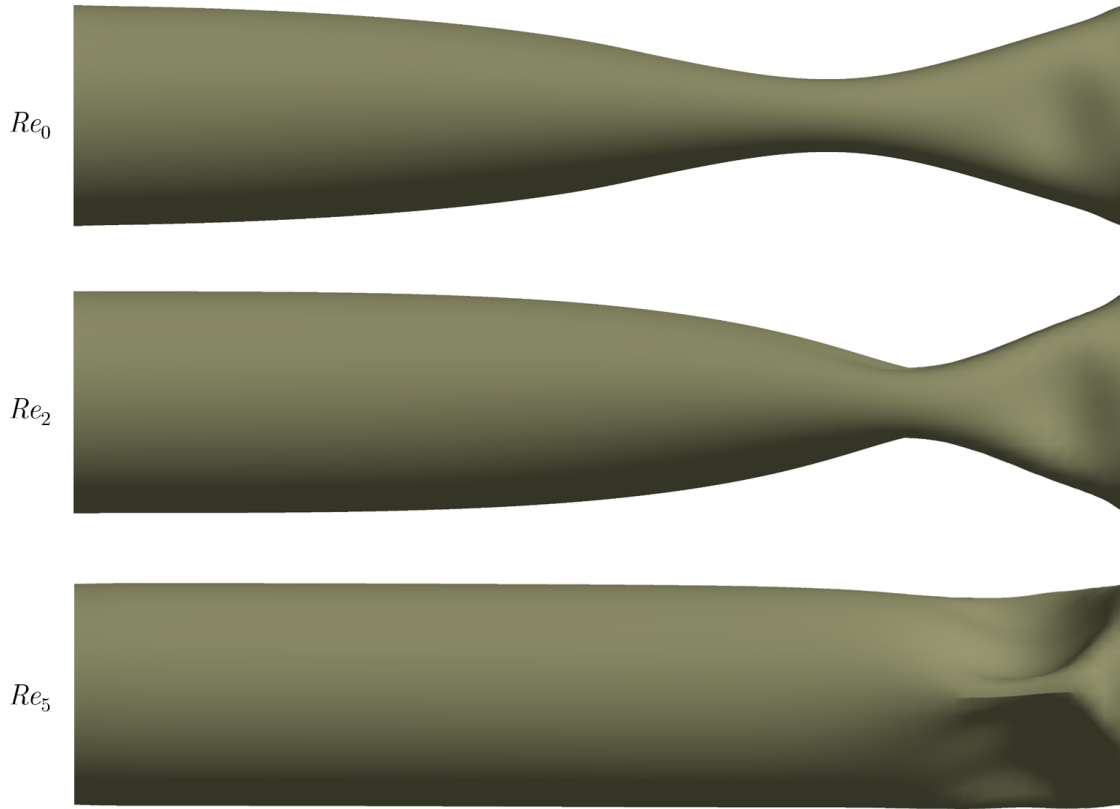


Figure 5.14: Comparison of tube deformations for the different Reynolds number cases, viewed from the y-z-plane. Images used courtesy of ANSYS, Inc.

should first be done. The same meshes were used for all the cases. It is possible that the fluid mesh was not sufficiently fine in the higher Reynolds number cases, as increased Reynolds numbers usually require more cells to reduce the numerical error.

Previous researchers have utilized symmetry when modelling the collapsible tube [30, 45] in order to reduce the required computational effort. However, the downside of using symmetry is that it does not allow the tube to buckle in all modes. If symmetry around the y-z-plane and the x-z-plane had been used in the current model, the 3-mode buckling in the Re_5 -case would not appear. It shows that symmetry should not be applied if the buckling mode is not already known before running the simulation or if the buckling mode is not symmetrical about any planes.

Evaluation of using a laminar flow model

Ku (1997) [38] reported that the critical upstream Reynolds number for turbulence is around 300 in stenotic flows (flow through narrowed arteries). A reason why turbulence occurs at such low Reynolds numbers could be the development of a shear layer between the central jet and separated recirculation zone [38]. As the Re_2 -case has a Reynolds number of 256 at the inlet, it is not far from the critical Reynolds number reported by Ku [38]. In addition, a central jet with recirculation zones can be observed in Fig. 5.11. The Re_2 -case was, therefore, run again with turbulence

modelling ($k - \omega$ SST model). When comparing the laminar and $k - \omega$ SST models, the resulting maximum tube deformations and centerline pressure profiles are almost identical. The largest difference in pressure along the tube centerline was located at the lowest pressure point and was 3% of the lowest value. The effect on the pressure is therefore small when considering turbulence or not. In addition, the turbulent viscosity is smaller than the dynamic viscosity everywhere except for a small area around the centerline close to the inlet.

A further investigation of the impact of modelling turbulence would be of interest for higher Reynolds number cases because turbulence, when of sufficient significance, can change the pressure distribution in the tube and hence the entire FSI problem. In addition, modelling turbulence can change how the flow separation is predicted. Turbulence may be of some significance in this case, but it is possible that the model does not sufficiently capture its effects.

The turbulence model, $k - \omega$ SST, was chosen arbitrarily, and it is possible that other RANS (Reynolds-averaged Navier Stokes) models are more suitable in this case. $k - \omega$ SST is, however, known to give better flow separation prediction than other RANS models and to provide high accuracy compared to its computational cost [36]. In order to make any conclusions on the importance of including turbulence modelling, a more detailed investigation of different turbulence models must be done. Potential transitional flow between laminar and turbulent flow should also be considered. Menter [47] mentioned that if RANS models are to be used in transitional flow, a proper formulation of the model is important to capture the effects. In addition to investigating the types of turbulence models, the mesh needs to be looked into to ensure the resolution is good enough for the chosen turbulence model.

Chapter 6

Conclusions

A numerical fluid-structure interaction model of flow through a collapsible tube has been created within Ansys Workbench [12] using a partitioned approach. The fluid-structure interaction is done through data transfer of interface properties via Ansys System Coupling [11]. The fluid and solid domains are solved separately, with Ansys Fluent [5], and Ansys Mechanical [8], respectively. The solid consists of linear elastic material, and the steady laminar fluid flow has Reynolds number 128.

Results in excellent agreement with previous numerical research [30, 33, 45] have been obtained. A qualitative comparison with experiments has also been made to evaluate the physicality of the tube deformation pattern and fluid flow development. As seen in experiments, the tube deformed closer to the downstream part of the flexible tube part, and the fluid flow velocity obtains a jet-like profile in the most deformed part and downstream of it.

One of the main challenges with modelling the system was ensuring the fluid mesh quality did not become too poor with large deformations. Due to the large deformations of the tube, the fluid mesh must be deformed accordingly. This is done with the Dynamic Mesh functionality in Ansys Fluent [5]. The mesh quality became slightly reduced from the initial mesh to the final deformed configuration, but a good mesh quality still remained.

The convergence and stability of data transfers have been looked into. The stability was improved by applying an under-relaxation factor to the transfer of forces from the fluid to the solid. The effect of changing the data transfer convergence was also investigated, showing little difference in the results when the RMS criteria were increased from 0.01 to 0.5.

In addition to verifying the model, the model was tested with increased Reynolds numbers ($Re_0 = 128$, $Re_2 = 256$, $Re_5 = 640$), resulting in an expected deformation trend. The largest deformation is obtained closer to the downstream end of the tube with increasing Reynolds numbers. In addition, the mode of tube buckling increased from 2 to 3 for the highest Reynolds number case, Re_5 .

The background for this thesis is related to OSA. Eventually, the goal is to predict the outcome of surgery in patients by numerically modelling the event of OSA,

which is a collapse in the upper airways. However, the upper airways are more complicated than the simple tube problem. In order to create an FSI model of the upper airways in Ansys Workbench [12], a more advanced model must be created. Although, creation of an advanced upper airway FSI model will require more work than simply modifying parameters of the current model, the good agreement with previous research has shown that FSI with large deformations in collapsible tubes can be done within Ansys Workbench [12], a partitioned and commercial FSI solver.

Chapter 7

Suggestions for future work

As mentioned in the introduction, the value of solving this FSI problem with commercial software is, amongst other reasons, that the model can be modified and developed for biological applications. As the model showed great agreement with previous numerical studies, suggestions for future work will be presented here.

7.1 Future work on current model

There are still many aspects to explore of the current collapsible tube problem, and some have already been mentioned in the results and discussion. An overview of aspects that should be investigated further in order to make the model more efficient and accurate is displayed in the list below.

- In Ansys System Coupling [11]:
 - Optimization of under-relaxation factor.
 - Optimization of coupling step size.
 - The two points mentioned above should also be investigated simultaneously as the optimal under-relaxation factor will vary with the coupling step size.
 - Investigate the effect on the solution with different coupling step sizes.
 - Investigate the effect of other stabilization techniques (other than under-relaxation), i.e., ramping and the Quasi-Newton method.
- In Ansys Fluent [5]:
 - Investigate the effects of changing the numerical schemes of the fluid flow.
 - Further investigation of dynamic mesh options.
 - Further investigation of turbulence modelling, both in terms of efficiency compared to using laminar models and the effect of including turbulence modelling in higher Reynolds number cases.

- In Ansys Mechanical [8]
 - Investigate the effect of changing from shell to solid elements.
 - Investigate the effect of analysis settings that have not been focused on in this work, such as stabilization and weak springs.

When these factors are investigated, the different results should be compared to the works of Hazel and Heil [30], Marzo et al. [45], and Huang [33], in order to determine the causes for the observed deviations in Fig. 5.1 and 5.2.

Oscillations that occur in collapsible tubes have not been given attention in this thesis. As has been observed in experiments, self-excited oscillations can occur in collapsible tube problems. Therefore, solving the same problem as fully transient would give more profound insights into the collapsible tube problem and might reveal other time-dependent phenomena not captured in the current model.

The limitations of Ansys [12] in terms of how close to collapse the tube can get should also be investigated. In such cases, the limiting part of the simulation will likely be to handle the gradually reducing and eventually diminishing fluid mesh in the most collapsed part. The fluid-structure interface will also need to be handled cautiously in such a case. It is possible that desired results, for instance, in the case of modelling the event of OSA, can be obtained without a complete collapse. However, testing how close to complete collapse it is possible to get to within Ansys Workbench [12] will give valuable insights into the software's capabilities.

In addition, conducting experiments with similar non-dimensional parameters and boundary conditions as the setup would be of great value in validating the model.

Collapsible tubes with even higher Reynolds numbers than those considered in this thesis should be simulated and investigated with turbulence modelling because it will be important when modelling the airflow in the upper airways. New mesh refinement studies should be done in such cases.

7.2 Developing more complex models

As the VirtuOSA project's final goal is to predict the effect of surgical intervention in OSA patients, the effect of including FSI in numerical modelling of the upper airways should be considered. Since FSI problems are significantly more computationally expensive than single-field analysis, it would be valuable to analyze the difference in flow properties when flow in the upper airways is modelled with rigid walls compared to when modelled with flexible walls. Although the effect of FSI will likely vary in different patients, such a study can provide insight into how valuable FSI is in this case compared to the added computational expense. In order to be able to conduct such studies, more complex models than the one created for this thesis must be created. The list below includes suggestions for how the model can be modified in order to behave more like the upper airways:

- Change material model, tube thickness, and length to obtain similar properties to the upper airways.
- Use air as the fluid, with a similar Reynolds number as during breath.
- Implement a realistic and transient breathing pattern.
- Change the external pressure on the tube to be similar to what the upper airways experience during sleep.
- Replace tube geometry with upper airway geometry.

It should be noted that the changes suggested are not easily implemented, not only because of the great challenge of creating such numerical models but also because accurate data on airway properties, such as material models and breathing pattern, can be challenging to obtain. Gradual implementation of the changes and simplifying assumptions will likely be necessary for developing such models.

Bibliography

- [1] ADINA. (2021). *ADINA FSI*. Retrieved December 11, 2021, from <http://www.adina.com/adina-fsi.shtml>
- [2] Akbar, B. (2021). Mathematical modelling and simulation of airflow in collapsible flow channels. *Project work, NTNU*.
- [3] *Ansys CFD-Post, 2021R2, CFD-Post User's guide*. (2021). ANSYS, Inc.
- [4] *Ansys Fluent, 2021R2, Theory Guide*. (2021). ANSYS, Inc.
- [5] *Ansys Fluent, 2021R2, User's Guide*. (2021). ANSYS, Inc.
- [6] *Ansys Mechanical, 2021R2, Structural Analysis Guide*. (2021). ANSYS, Inc.
- [7] *Ansys Mechanical, 2021R2, Theory Guide*. (2021). ANSYS, Inc.
- [8] *Ansys Mechanical, 2021R2, User Guide*. (2021). ANSYS, Inc.
- [9] *Ansys Meshing, 2021R2, ANSYS Meshing User's Guide*. (2021). ANSYS, Inc.
- [10] *Ansys Spaceclaim, 2021R2, Discovery Spaceclaim*. (2021). ANSYS, Inc.
- [11] *Ansys System Coupling, 2021R2, User's Guide*. (2021). ANSYS, Inc.
- [12] *Ansys Workbench, 2021R2, User's Guide*. (2021). ANSYS, Inc.
- [13] Antic, N. A., Catcheside, P., Buchan, C., Hensley, M., Naughton, M. T., Rowland, S., Williamson, B., Windler, S. & McEvoy, R. D. (2011). The effect of CPAP in normalizing daytime sleepiness, quality of life, and neurocognitive function in patients with moderate to severe OSA. *Sleep*, 34(1), 111–119. <https://doi.org/10.1093/sleep/34.1.111>
- [14] Bazilevs, Y., Takizawa, K. & Tezduyar, T. E. (2013). *Computational fluid-structure interaction: Methods and applications*. John Wiley & Sons.
- [15] Bertram, C. & Castles, R. (1999). Flow limitation in uniform thick-walled collapsible tubes. *Journal of Fluids and Structures*, 13(3), 399–418. <https://doi.org/10.1006/jfls.1999.0207>
- [16] Bertram, C. & Godbole, S. (1997). LDA measurements of velocities in a simulated collapsed tube. *Journal of Biomechanical Engineering*. <https://doi.org/10.1115/1.2796101>
- [17] Bertram, C., Raymond, C. & Butcher, K. (1989). Oscillations in a collapsed-tube analog of the brachial artery under a sphygmomanometer cuff. *Journal of Biomechanical Engineering*. <https://doi.org/10.1115/1.3168364>
- [18] Buriev, B., Kim, T.-D. & Seo, T.-W. (2009). Fluid-structure interactions of physiological flow in stenosed artery. *Korea-Australia Rheology Journal*, 21(1), 39–46.
- [19] Celik, I., Ghia, U., Roache, P., Freitas, C., Coleman, H. & Raad, P. (2000). Journal of Fluids Engineering Editorial Policy Statement on the Control of Numerical Accuracy.

-
- [20] Chang, K. K., Kim, K. B., McQuilling, M. W. & Movahed, R. (2018). Fluid structure interaction simulations of the upper airway in obstructive sleep apnea patients before and after maxillomandibular advancement surgery. *American Journal of Orthodontics and Dentofacial Orthopedics*, 153(6), 895–904. <https://doi.org/10.1016/j.ajodo.2017.08.027>
 - [21] Chimakurthi, S. K., Reuss, S., Tooley, M. & Scampoli, S. (2018). ANSYS Workbench System Coupling: a state-of-the-art computational framework for analyzing multiphysics problems. *engineering with Computers*, 34(2), 385–411. <https://doi.org/10.1007/s00366-017-0548-4>
 - [22] Chouly, F., Van Hirtum, A., Lagrée, P.-Y., Pelorson, X. & Payan, Y. (2008). Numerical and experimental study of expiratory flow in the case of major upper airway obstructions with fluid–structure interaction. *Journal of Fluids and Structures*, 24(2), 250–269. <https://doi.org/10.1016/j.jfluidstructs.2007.08.004>
 - [23] Comsol. (2018). *FEM vs. FVM*. Retrieved December 14, 2021, from <https://www.comsol.com/blogs/fem-vs-fvm/>
 - [24] Degroote, J., Swillens, A., Bruggeman, P., Haelterman, R., Segers, P. & Vierendeels, J. (2010). Simulation of fluid–structure interaction with the interface artificial compressibility method. *International Journal for Numerical Methods in Biomedical Engineering*, 26(3–4), 276–289. <https://doi.org/10.1002/cnm.1276>
 - [25] Ezkurra Mayor, M., Esnaola Ramos, J. A., Martinez Aguirre, M., Lertxundi, U. & Etxeberria, U. (2018). Analysis of one-way and two-way FSI approaches to characterise the flow regime and the mechanical behaviour during closing manoeuvring operation of a butterfly valve. *World Academy of Science, Engineering and Technology*.
 - [26] Flaherty, J. E., Keller, J. B. & Rubinow, S. (1972). Post buckling behavior of elastic tubes and rings with opposite sides in contact. *SIAM Journal on Applied Mathematics*, 23(4), 446–455. <https://doi.org/10.1137/0123047>
 - [27] Griffith, B. E. & Patankar, N. A. (2020). Immersed methods for fluid–structure interaction. *Annual Review of Fluid Mechanics*, 52, 421–448. <https://doi.org/10.1146/annurev-fluid-010719-060228>
 - [28] Grotberg, J. B. & Jensen, O. E. (2004). Biofluid mechanics in flexible tubes. *Annual Review of Fluid Mechanics*, 36, 121–147. <https://doi.org/10.1146/annurev.fluid.36.050802.121918>
 - [29] Ha, S. T., Ngo, L. C., Saeed, M., Jeon, B. J. & Choi, H. (2017). A comparative study between partitioned and monolithic methods for the problems with 3D fluid-structure interaction of blood vessels. *Journal of Mechanical Science and Technology*, 31(1), 281–287. <https://doi.org/10.1007/s12206-016-1230-2>
 - [30] Hazel, A. L. & Heil, M. (2003). Steady finite-reynolds-number flows in three-dimensional collapsible tubes. *Journal of Fluid Mechanics*, 486, 79–103. <https://doi.org/10.1017/S0022112003004671>
 - [31] Hirt, C. W., Amsden, A. A. & Cook, J. (1974). An arbitrary Lagrangian-Eulerian computing method for all flow speeds. *Journal of Computational Physics*, 14(3), 227–253. [https://doi.org/10.1016/0021-9991\(74\)90051-5](https://doi.org/10.1016/0021-9991(74)90051-5)
 - [32] Hou, G., Wang, J. & Layton, A. (2012). Numerical methods for fluid-structure interaction—a review. *Communications in Computational Physics*, 12(2), 337–377. <https://doi.org/10.4208/cicp.291210.290411s>
-

-
- [33] Huang, Q. (2020). *Low reynolds number turbulent FSI and its applications in biological flows* (Doctoral dissertation). The University of New South Wales.
 - [34] Ingram, D. M., Causon, D. M. & Mingham, C. G. (2003). Developments in Cartesian cut cell methods. *Mathematics and Computers in Simulation*, 61(3-6), 561–572. [https://doi.org/10.1016/S0378-4754\(02\)00107-6](https://doi.org/10.1016/S0378-4754(02)00107-6)
 - [35] Johansen, S. T. (2020). TEP4165 Lectures Chapter XI: FVM for steady state diffusion problems. *NTNU*.
 - [36] *K-Omega and K-Omega SST*. (2021). Retrieved June 8, 2022, from <https://www.simscale.com/docs/simulation-setup/global-settings/k-omega-sst/>
 - [37] Koh, W., Kang, S., Cho, M. & Yoo, J. Y. (2009). Three-dimensional steady flow in non-linear elastic collapsible tubes. *Fluids Engineering Division Summer Meeting, 43727*, 1785–1790. <https://doi.org/10.1115/FEDSM2009-78343>
 - [38] Ku, D. N. (1997). Blood flow in arteries. *Annual review of fluid mechanics*, 29(1), 399–434. <https://doi.org/10.1146/annurev.fluid.29.1.399>
 - [39] Lambeth, C., Kolevski, B., Amis, T. & Kairaitis, K. (2017). Feedback modulation of surrounding pressure determines the onset of negative effort dependence in a collapsible tube bench model of the pharyngeal airway. *Journal of Applied Physiology*, 123(5), 1118–1125. <https://doi.org/10.1152/jappphysiol.00378.2017>
 - [40] Le, T. B., Moghaddam, M. G., Woodson, B. T. & Garcia, G. J. (2019). Air-flow limitation in a collapsible model of the human pharynx: Physical mechanisms studied with fluid-structure interaction simulations and experiments. *Physiological Reports*, 7(10). <https://doi.org/10.14814/phy2.14099>
 - [41] LSTC. (n.d.). *LS-DYNA*. Retrieved December 15, 2021, from <https://www.lstc.com/products/lis-dyna>
 - [42] Luo, X. (2015). Modelling flows in collapsible tubes. *Encyclopedia of Life Support Systems (EOLSS)*, 213–240.
 - [43] Luo, X. & Pedley, T. (1995). A numerical simulation of steady flow in a 2-D collapsible channel. *Journal of Fluids and Structures*, 9(2), 149–174. <https://doi.org/10.1006/jfls.1995.1008>
 - [44] Luo, X. & Pedley, T. (1996). A numerical simulation of unsteady flow in a two-dimensional collapsible channel. *Journal of Fluid Mechanics*, 314, 191–225. <https://doi.org/10.1017/S0022112096000286>
 - [45] Marzo, A., Luo, X. & Bertram, C. (2005). Three-dimensional collapse and steady flow in thick-walled flexible tubes. *Journal of Fluids and Structures*, 20(6), 817–835. <https://doi.org/10.1016/j.jfluidstructs.2005.03.008>
 - [46] MATLAB. (2021). *Version 9.10.0.1602886 (r2021a)*. The MathWorks Inc.
 - [47] Menter, F. R., Langtry, R. & Völker, S. (2006). Transition modelling for general purpose cfd codes. *Flow, turbulence and combustion*, 77(1), 277–303. <https://doi.org/10.1007/s10494-006-9047-1>
 - [48] Non-linear finite element analysis. (2003). In *Structural integrity and reliability in electronics: Enhancing performance in a lead-free environment* (pp. 305–318). Springer Netherlands. https://doi.org/10.1007/1-4020-2611-0_17
 - [49] *OpenFOAM*. (n.d.). Retrieved June 8, 2022, from www.openfoam.org
 - [50] Owens, R. L., Edwards, B. A., Sands, S. A., Butler, J. P., Eckert, D. J., White, D. P., Malhotra, A. & Wellman, A. (2014). The classical Starling resistor model often does not predict inspiratory airflow patterns in the human upper airway.
-

- Journal of Applied Physiology*, 116(8), 1105–1112. <https://doi.org/10.1152/jappphysiol.00853.2013>
- [51] Pasquariello, V., Hammerl, G., Örley, F., Hickel, S., Danowski, C., Popp, A., Wall, W. A. & Adams, N. A. (2016). A cut-cell finite volume–finite element coupling approach for fluid–structure interaction in compressible flow. *Journal of Computational Physics*, 307, 670–695. <https://doi.org/10.1016/j.jcp.2015.12.013>
- [52] Peskin, C. S. (1972). Flow patterns around heart valves: A numerical method. *Journal of Computational Physics*, 10(2), 252–271. [https://doi.org/10.1016/0021-9991\(72\)90065-4](https://doi.org/10.1016/0021-9991(72)90065-4)
- [53] Pirnar, J., Dolenc-Grošelj, L., Fajdiga, I. & Žun, I. (2015). Computational fluid-structure interaction simulation of airflow in the human upper airway. *Journal of Biomechanics*, 48(13), 3685–3691. <https://doi.org/10.1016/j.jbiomech.2015.08.017>
- [54] *Plane stress/plane strain stiffness equations*. (n.d.). Memphis University. Retrieved May 13, 2022, from http://www.ce.memphis.edu/7117/notes/presentations/chapter_06b.pdf
- [55] *Plate bending elements*. (n.d.). Memphis University. Retrieved May 13, 2022, from http://www.ce.memphis.edu/7117/notes/presentations/chapter_12.pdf
- [56] Raback, P., Ruokolainen, J., Lyly, M. & Järvinen, E. (2001). Fluid-structure interaction boundary conditions by artificial compressibility. *ECCOMAS CFD, 2001*.
- [57] Rast, M. P. (1994). Simultaneous solution of the Navier-Stokes and elastic membrane equations by a finite element method. *International Journal for Numerical Methods in Fluids*, 19(12), 1115–1135. <https://doi.org/10.1002/flid.1650191205>
- [58] Sankar, V. & Meyers, A. (2011). Physiologic approach in snoring and obstructive sleep apnea.
- [59] Schwartz, A. R. & Smith, P. L. (2013). Crosstalk proposal: The human upper airway does behave like a Starling resistor during sleep. *The Journal of Physiology*, 591(Pt 9), 2229. <https://doi.org/10.1113/jphysiol.2012.250654>
- [60] Scroggs, R. A. (2002). *Validation of computational fluid-structure interaction models by comparison with collapsible tube experiments*. (Doctoral dissertation). University of Sheffield.
- [61] Shapiro, A. H. (1977). Steady flow in collapsible tubes. *Journal of Biomechanical Engineering*. <https://doi.org/10.1115/1.3426281>
- [62] Sintef. (2021). *Virtual Surgery in the Upper Airways - New Solutions to Obstructive Sleep Apnea Treatment (VirtuOSA)*. Retrieved May 29, 2022, from <https://www.sintef.no/en/projects/2020/virtuosa-virtual-surgery-in-the-upper-airways-new-solutions-to-obstructive-sleep-apnea-treatment/>
- [63] Smith, M. (2009). *Abaqus/standard user's manual, version 6.9*. Dassault Systèmes Simulia Corp.
- [64] Subramaniam, D. R., Mylavarapu, G., Fleck, R. J., Amin, R. S., Shott, S. R. & Gutmark, E. J. (2017). Effect of airflow and material models on tissue displacement for surgical planning of pharyngeal airways in pediatric down syndrome patients. *Journal of the Mechanical Behavior of Biomedical Materials*, 71, 122–135. <https://doi.org/10.1016/j.jmbbm.2017.03.007>

- [65] Tang, D., Yang, C., Kobayashi, S. & Ku, D. N. (2004). Effect of a lipid pool on stress/strain distributions in stenotic arteries: 3-D fluid-structure interactions (FSI) models. *Journal of Biomechanical Engineering*, 126(3), 363–370. <https://doi.org/10.1115/1.1762898>
- [66] Vassen, J.-M., DeVincenzo, P., Hirsch, C. & Leonard, B. (2011). Strong coupling algorithm to solve fluid-structure-interaction problems with a staggered approach. *7th European Symposium on Aerothermodynamics*, 692, 128.
- [67] Versteeg, H. K. & Malalasekera, W. (1995). *An introduction to computational fluid dynamics: The finite volume method*.
- [68] Wang, W. & Yan, Y. (2010). Strongly coupling of partitioned fluid–solid interaction solvers using reduced-order models. *Applied Mathematical Modelling*, 34(12), 3817–3830. <https://doi.org/10.1016/j.apm.2010.03.022>
- [69] *What happens during OSA*. (2011). Harvard Medical School. Retrieved December 5, 2021, from <https://healthysleep.med.harvard.edu/sleep-apnea/what-is-osa/what-happens>
- [70] Young, D. (1979). Fluid mechanics of arterial stenoses.
- [71] Zhang, H., Zhang, X., Ji, S., Guo, Y., Ledezma, G., Elabbasi, N. & DeCougny, H. (2003). Recent development of fluid–structure interaction capabilities in the ADINA system. *Computers & Structures*, 81(8-11), 1071–1085. [https://doi.org/10.1016/S0045-7949\(03\)00009-9](https://doi.org/10.1016/S0045-7949(03)00009-9)
- [72] Zhang, S., Luo, X. & Cai, Z. (2018). Three-dimensional flows in a hyperelastic vessel under external pressure. *Biomechanics and Modeling in Mechanobiology*, 17(4), 1187–1207. <https://doi.org/10.1007/s10237-018-1022-y>
- [73] Zhu, Y., Luo, X., Wang, H., Ogden, R. & Berry, C. (2012). Nonlinear buckling of three-dimensional thick-walled elastic tubes under pressure. *International Journal of Non-Linear Mechanics*. <https://doi.org/10.1016/j.ijnonlinmec.2012.06.013>

Appendix A

Details of main case model setup in ANSYS Workbench

The purpose of this appendix is to provide a sufficiently detailed guide for the reader to be able to recreate the model. This appendix is structured so that the reader can follow the steps chronologically. It is assumed that the reader already has basic knowledge and experience with the software involved.

System setup

First, drag and connect the four systems needed in ANSYS Workbench as displayed in Fig. A.1.

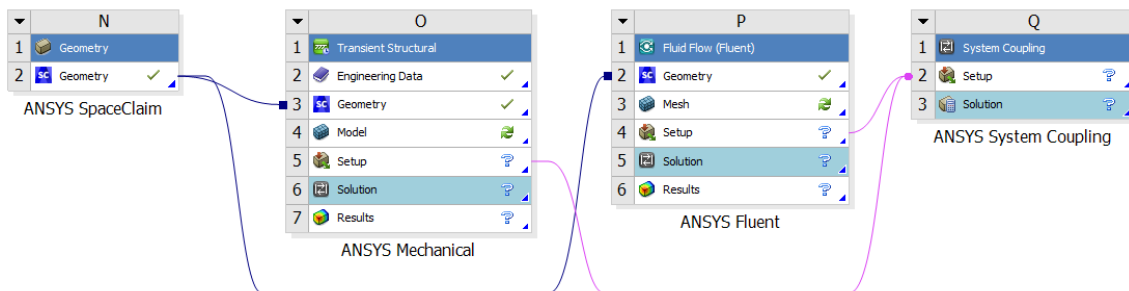


Figure A.1: Systems and setup used in Ansys Workbench [12]. Image used courtesy of ANSYS, Inc.

Geometry

Open the Geometry system and create the fluid and solid domains in the same SpaceClaim file:

- Create the fluid domain by making a cylinder body with radius, $R = 0.5m$



Figure A.2: Geometry in Ansys SpaceClaim [10], viewed from the y-z-plane. Image used courtesy of ANSYS, Inc.

and length, $L_{up} + L_{flex} + L_{down} = 10.5m$.

- Divide the fluid wall surface into three parts in the streamwise direction to correspond to the three parts of the tube (rigid, flexible, rigid).
- Create the solid domain (only flexible part) by making a cylindrical surface outside the fluid domain where the flexible part is supposed to be. The radius of this surface is $R + h/2$ because when the thickness h is later applied to meshing, it will thicken from the location of the surface, i.e., $h/2$ on both sides. This way, it will, in practice, meet the fluid wall. (i.e., no thickness of the cylindrical shell). See Fig. A.2 to view how the solid surface (dark grey) is placed compared to the fluid (blue).

Transient Structural

Define solid material properties in Engineering data

Next, move to the Transient Structural system and open Engineering Data (O2 in Fig. A.1). Create a new material and insert the values for material density, E-modulus, and Poisson ratio as in Fig. A.3.

1	Property	Value	Unit		
2	Material Field Variables	Table			
3	Density	1000	kg m ⁻³		
4	Isotropic Elasticity				
5	Derive from	Young's Modulus an...			
6	Young's Modulus	4559.4	Pa		
7	Poisson's Ratio	0.49			
8	Bulk Modulus	75990	Pa		
9	Shear Modulus	1530	Pa		

Figure A.3: Defining the tube material in Engineering Data in Ansys Workbench [12]. Image used courtesy of ANSYS, Inc.

Creation of the solid model

Open the Model-cell in Transient Structural (O4 in Fig. A.1).

- In Geometry, suppress the fluid geometry and assign the tube surface the newly created material. Also set the following for the surface:
 - Model Type: Shell
 - Stiffness Behaviour: Flexible
 - Stiffness Option: Membrane and Bending
 - Thickness: $0.025m$
 - Nonlinear Effects: Yes
- In Mesh, choose:
 - Physics Preference: Nonlinear Mechanical
 - Element Order : Quadratic
 - Element size: $0.1m$
- In Transient:
 - In Analysis Settings, insert as in Fig. A.4.
 - Insert the following supports and loads:
 - * Pressure: Normal to surface with magnitude = $-1.4 \cdot \text{time}$
 - * Pressure: Normal to surface with magnitude = $-(0.014 - 0.50794 \cdot x \cdot x) \cdot (1 - \text{time})$
 - * Fixed Support: On both ends of tube (edges)
 - * Fluid Solid Interface: On surface

Details of "Analysis Settings"	
[-] Step Controls	
Number Of Steps	1.
Current Step Number	1.
Step End Time	2. s
Auto Time Stepping	On
Define By	Time
Initial Time Step	1.e-004 s
Minimum Time Step	1.e-008 s
Maximum Time Step	0.1 s
Time Integration	Off
[-] Solver Controls	
Solver Type	Program Controlled
Weak Springs	On
Spring Stiffness	Program Controlled
Large Deflection	On
App. Based Settings	Moderate Speed Dynamics
[+] Restart Controls	
[-] Nonlinear Controls	
Newton-Raphson Option	Unsymmetric
Force Convergence	Program Controlled
Moment Convergence	Program Controlled
Displacement Convergence	Program Controlled
Rotation Convergence	Program Controlled
Line Search	On
Stabilization	Constant
--Method	Damping
--Damping Factor	5.e-002
--Activation For First Substep	Yes
--Stabilization Force Limit	0.2

Figure A.4: Analysis Settings in Ansys Mechanical [8]. Image used courtesy of ANSYS, Inc.

Fluid Flow (Fluent)

Mesh

Move to the Fluid Flow (Fluent)- system in Workbench and open Mesh (P3 in Fig. A.1).

- Suppress the solid surface.
- In Mesh:
 - Choose:
 - * Physics Preference: CFD
 - * Solver Preference: Fluent

- * Element Order: Quadratic
- * Element size. 0.05 m
- Insert:
 - * Patch Conforming Method: Tetrahedrons
 - * Inflation: On fluid volume with boundary on the wall surface. Transition Ratio = 0.25. Maximum Layers = 3. Growth Ratio: 1.2
- Name selections (inlet, outlet, fluid volume, flexible wall and rigid walls)

Creation of the fluid model

Open Setup in Fluid Flow (Fluent) (P3 in Fig. A.1).

General settings and Models

In General make sure solver is set to be Pressure-Based and Steady. In Models, choose Laminar. In Monitors, set all residual criteria to 10^{-5} .

Create fluid material and assign it to the fluid domain

In Materials, create a new fluid with constant density, $1kg/m^3$ and constant viscosity, $0.00395288kg/(ms)$. In Cell Zone Conditions, assign the fluid volume the new fluid.

Set boundary conditions

In Boundary Conditions:

- For Inlet: Choose velocity-inlet with Velocity Specification Method called Components. For Z-velocity insert the expression: $1.01193843638015 [m\ s^{-1}] * (1-4*(x^{**2}+y^{**2})/(1[m]^{**2}))$
- For Outlet: Choose pressure-outlet with Gauge Pressure = $0Pa$.

Activate dynamic mesh

In Dynamic Mesh, tick off Dynamic Mesh. Then, in Mesh Methods, tick off Smoothing and Remeshing, open Settings and:

- For Smoothing settings, make sure Diffusion smoothing is chosen. Go to Advanced Settings and choose Diffusion Parameter = 3. Choose Maximum Number of Iterations = 500.

- For Remeshing settings, make sure Unified Remeshing is chosen. Go to Advanced Settings and tick off Retain Size Distribution.

Create a new Dynamic Mesh Zone by clicking on Create/Edit. Here choose the fluid surface in contact with the flexible wall and assign it with type System Coupling.

Choose methods

In Methods, choose:

- Pressure Velocity Coupling Scheme: Coupled
- Spatial Discretization
 - Gradient: Least Squares Cell Based
 - Pressure: Second Order
 - Momentum: Second Order Upwind

Run calculation

In Run Calculation, keep the default settings, but change the number of iterations to 1000.

System Coupling

In the System Coupling-System, right-click on Setup (C2 in Fig. A.1) and choose Update. Then open Setup.

Couple participants

Couple the participants by marking the Fluid Solid Interface created in Mechanical and the dynamic mesh surface from Fluent simultaneously. Click on Create Data Transfer. The software will automatically create a two-way transfer between the surfaces, transferring forces from the fluid to the solid (Data Transfer 1) and displacements from solid to fluid (Data Transfer 2).

Under-relaxation

In Data Transfer 1, write in an under-relaxation factor of 0.3.

Analysis settings

Since the displacements are small when the first half of the external loading is applied, the time step can be larger in this period and the simulation should therefore be executed in two steps.

- Step 1: Choose End Time = 0.5, Step Size = 0.1, Minimum iterations = 1, Maximum Iterations = 40. Press update and let the simulation run until finished.
- Step 2: Choose Coupling Initialization = Step 5 Time 0.5 [s], End Time = 1. Step Size = 0.01, Minimum iterations = 1, Maximum Iterations = 40. Press update and let the simulation run until finished.

Appendix B

Abstract accepted to ESB 2022

The paper "Simulation of Fluid-Structure Interaction of Flow in Collapsible Tubes: A Simplified Model for Obstructive Sleep Apnea" by Batool Akbar, Sverre Gulikstad Johnsen, Paul Roger Leinan, and Bernhard Müller has been accepted by the 27th Congress of the European Society of Biomechanics. The work will be presented at ESB 2022, a biomechanics conference in Porto, Portugal, by Batool Akbar.

SIMULATION OF FLUID-STRUCTURE INTERACTION OF FLOW IN COLLAPSIBLE TUBES: A SIMPLIFIED MODEL FOR OBSTRUCTIVE SLEEP APNEA

Batool Akbar (1), Sverre Gullikstad Johnsen (2), Paul Roger Leinan (2), Bernhard Müller (1)

1. NTNU, Dept. Energy and Process Engineering, Norway; 2. SINTEF Industry, Norway

Introduction

Obstructive Sleep Apnea (OSA) is a common sleeping disorder which momentarily blocks the airflow in the upper airways, causing breathing to stop during sleep. OSA can lead to significant reduction of sleep quality, as well as more serious health issues [1]. One way of mitigating events of OSA is the use of a continuous positive airway pressure (CPAP) device during the night. Surgical intervention is another mitigation technique. However, medical doctors and surgeons, will in most cases not know if surgery will lead to improving, no change or worsening of the patients' sleep apnea. Researchers have therefore tried to numerically simulate processes in the upper airways as an attempt to get a better understanding of what happens in the airways during sleep apnea, in order to eventually more accurately predict the outcome of surgery.

It is believed that the Venturi effect occurring in the narrow passages in the upper airways is responsible for the onset of OSA. The logic behind this statement is that some parts of the upper airways consist of soft, collapsible tissue and when air flows through these parts, the pressure difference between the inside and outside of the airway can lead to deformation of the soft tissue, making the airway even narrower, eventually leading to collapse. Because there is a strong dependency between the behavior of the tissue and the air flowing through, fluid-structure interaction (FSI) is necessary to be considered when simulating such events numerically. In the current work, two-way FSI simulations have been conducted for a simplified geometry of the upper airways using commercial software.

Method

Two-way FSI simulations of collapse of a flexible tube have been created using ANSYS Workbench 2021 R1. ANSYS Fluent and ANSYS Mechanical are used to solve the governing equations of the fluid and solid, respectively. ANSYS System Coupling is used to transfer data between the fluid and solid domains, creating the partitioned fluid-structure interaction.

The solid was modelled as a hyperelastic material using the Arruda-Boyce model [2]. Initial validation of

the solid model was performed excluding the fluid domain. Two airflow scenarios were investigated: 1) initially stagnant flow being displaced by the solid deformation; and 2) constant predefined air flow.

Results and Discussion

The structural model has been compared with experimental and numerical results by Zarandi et al. [3], displaying good agreement. Figure 1 shows the deformation of the solid and fluid after the tube has been exposed to external pressure, when the fluid is initially stagnant (scenario 1). Reasonable qualitative results, in accordance with results by Scroggs [4], have also been obtained when the fluid was given an inlet velocity.

Results to be obtained from these models will give insight into what happens with both the fluid flow and the material in collapsible tubes. Due to the similarity with the upper airways, it is reasonable to believe that trends and results from this model can be translated to the upper airways. Furthermore, once the model has been validated, it will be possible to change the model for it to be more realistic in terms of representing the behavior of the upper airways during OSA. This work forms a basis for ongoing studies on how to use commercial simulation software in the development of computer-aided decision support-tools for patient specific OSA treatment. In the future, we foresee that such tools can be used to evaluate patient specific treatment options. The ultimate goal is to reduce risk and inconvenience for patients and societal costs by providing the optimal treatment.

References

1. Tarek Gharibeh and Reena Mehra. Nature and Science of Sleep, 2:233, 2010.
2. Ellen M Arruda and Mary C Boyce. Journal of the Mechanics and Physics of Solids, 41(2):389–412, 1993.
3. M Amin F Zarandi et al. Computers in Biology and Medicine, 136, 2021.
4. Richard A Scroggs. PhD thesis, University of Sheffield, 2002.

Acknowledgements

This work is a part of VirtuOSA (Virtual Surgery in the Upper Airways – New Solutions to Obstructive Sleep Apnea Treatment), which is a research collaboration between SINTEF, NTNU and St. Olavs hospital, Trondheim University Hospital, Norway. The project is mainly financed by the Research Council of Norway (RCN).

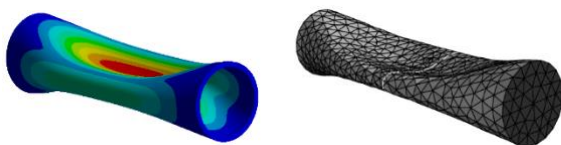


Figure 1 Deformed solid (left) and fluid domain (right).



